IMPERIAL

UNIVERSITÄT
HEIDELBERG
ZUKUNFT
SEIT 1386

Bragg Scattering of Quantum Gases for Spatially-Resolved Velocity Field Extraction

Author:
Louis Evans

Supervisor:
Prof. Dr. Markus Oberthaler

Submitted in fulfillment of the requirements for the degree of
Master of Science in Physics with a Year Abroad

Word Count: 9,803

June 2025

Abstract

This thesis presents novel Bragg scattering-based techniques to extract spatially-resolved velocity fields in quasi-2D Bose-Einstein condensates, enriching the study of quantum turbulence. An experimental Bragg scattering setup is implemented and characterised on stationary condensates. Two newfound methods; spectroscopic and broadband velocimetry, are introduced and used to extract spatially-resolved 1D velocity field projections for vortex–antivortex configurations, with experimental measurements in good agreement with computational results. Initial experimental results for the 2D velocity field extraction of a turbulent BEC are reported, offering a powerful new diagnostic tool for probing quantum turbulence.

Zusammenfassung

In der vorliegenden Arbeit werden neuartige, auf Bragg-Streuung basierende Verfahren zur Extraktion ortsaufgelöster Geschwindigkeitsfelder in quasi-2D Bose-Einstein-Kondensaten vorgestellt, wodurch die Untersuchung von Quantenturbulenz bereichert wird. Ein experimenteller Bragg-Streuaufbau wird implementiert und an stationären Kondensaten charakterisiert. Zwei neue Methoden – die spektroskopische und die breitbandige Velocimetrie – werden eingeführt und zur Bestimmung ortsaufgelöster 1D Projektionen des Geschwindigkeitsfelds von Vortex–Antivortex-Konfigurationen eingesetzt. Die experimentellen Messungen stimmen dabei gut mit numerischen Berechnungen überein. Erste experimentelle Ergebnisse zur Bestimmung des zweidimensionalen Geschwindigkeitsfelds eines turbulenten BECs werden vorgestellt, was ein leistungsstarkes neues Diagnosewerkzeug zur Untersuchung von Quantenturbulenz darstellt.

Acknowledgments

I would like to express my deepest gratitude to those who supported me throughout the course of this project. To Markus, for his energetic and enthusiastic supervision, and to the BECK team: Helmut, Marius, Nikolas, Elinor, Jelte, Philipp, and Hanyi. Thank you for the guidance provided in and out of the lab, for the many fascinating discussions, and for making Heidelberg feel like home. I will forever be grateful for such a wonderful group of guides to lead me into the world of experimental atomic physics.

Contents

List of Figures

1. Introduction

When a system of Bosons is cooled below a critical temperature, a Bose-Einstein condensate (BEC) is formed, where particles occupy the lowest energy state, resulting in a macroscopic effective wavefunction with a well-defined continuous phase at every point in space, $\phi(\boldsymbol{r})$. Since their experimental realisation in 1990 [1], atomic BECs have made for powerful analog quantum simulators due to their high level of controllability, and low level of noise. Just as a water tank can be used to investigate fluid dynamics, an atomic BEC provides a platform to probe the quantum dynamics that govern the universe at the smallest scale.

Far-from-equilibrium, turbulent quantum systems are of significant interest in analog quantum simulation [2–5]. In the description of classical turbulence, kinetic energy is distributed amongst circulating flow structures of continuous sizes [6]. In many-body quantum systems, flows are superfluid [7], and the velocity field depends on the particle mass m and the phase gradient:

$$\boldsymbol{v}(\boldsymbol{r}) = \frac{\hbar}{m}\boldsymbol{\nabla}\phi(\boldsymbol{r}) \quad . \tag{1.1}$$

The continuity of the phase profile results in the quantisation of angular momentum, where the phase accumulated around a vortex core must be an integer multiple of 2π. Therefore, the physics of quantum turbulence diverges from its classical counterpart. Quantised vortices and quantum turbulence govern a broad range of quantum phenomena, such as the resistive behaviour of superconductors [8], and pulsar glitches in neutron stars [9]. Recent theoretical work also maps quantised vortices in 2D BECs to 2D Maxwellian electrodynamics [10].

Historically, BECs are probed by destructively measuring the spatial distribution of atoms. This can be done immediately after an experiment to extract the instantaneous BEC density distribution, or after some phase space rotation [11], granting information of the atomic velocities at the sacrifice of spatial resolution. However, this is not sufficient for the investigation of quantum turbulence, where vortex vorticity cannot be inferred from spatial or velocity data alone. This requires the development of new techniques to extract spatially-resolved velocity field information.

In previous work, velocity-selective Bragg scattering along a single axis is used to spatially resolve atoms of a *single* class of 1D velocity projections along the axis [12–15]. This allows for the diagnosis of vorticity, and has resulted in key experimental breakthroughs, such as the observation of Onsager cluster formation [16], and the investigation of vortex collisions [17]. In this thesis, we introduce two novel methods for extracting the *full* 1D projected velocity field. *Spectroscopic* velocimetry can be used to extract the velocity field of a reproducible BEC configuration over multiple realisations. *Broadband* velocimetry enables velocity field extraction in a single shot, essential for studying irreproducible turbulent configurations. Finally, we present initial results for 2D velocity field extraction for the first time in quasi-2D atomic BEC experiments. Through this work, we provide new tools for the exploration of quantum turbulence in atomic BECs.

The thesis is structured as follows: Section 1.1 provides a brief overview of the BEC experiment, and methods used to generate out-of-equilibrium BEC configurations. Chapter 2 presents background theory of Bragg scattering as a velocity-selective, inelastic 2-photon transition between momentum states and outlines the 2 velocimetric methods. Chapter 3 describes the implemented experimental setup to produce two 'Bragg beams' capable of Bragg scattering along two axes. In Chapter 4, we characterise the interactions of a Bragg beam with a stationary condensate, establishing experimental parameters for velocity field extraction. In Chapter 5, we probe dynamic BECs. First, we establish velocity-dependence on a deterministic uniform velocity field. Then, we apply the newfound velocimetric methods to extract 1D velocity fields from vortex-antivortex configurations, and find that both methods extract velocity fields in good agreement with numerically simulated expectations. Finally, we present initial results for the 2D velocity field measurement of a turbulent vortex gas configuration. Chapter 6 provides future outlook and concluding remarks.

1.1 BECK Experiment Condensed

In the BECK lab, we perform quantum simulation on a potassium-39 BEC that is tightly confined in the gravity axis (z). All quantum dynamics of interest are observed in the perpendicular ($x-y$) plane. ^{39}K is a particularly interesting atomic species because s-wave scattering lengths can be tuned via an external magnetic field, effectively changing how strongly atoms repel each other [18]. The setup has been used to simulate wave propagation in curved spacetime [19] and particle production in the early universe [20]. Previous efforts to investigate quantum turbulence revealed supersolid-like sound modes in a driven BEC [21, 22].

1.1.1 Dipole Potentials

In a vacuum chamber, ^{39}K atoms are cooled, trapped, and condensed via a number of experimental protocols [23]. The condensed atoms are then manipulated using far-detuned laser light of frequency ω_l. This produces a spatially-varying dipole potential proportional to the light intensity:

$$U(\boldsymbol{r}) = -\frac{3\pi c^2 \Gamma}{2\omega_0^2 \Delta^2} I(\boldsymbol{r}) \quad , \tag{1.2}$$

where c is the speed of light, Γ is the linewidth of the electronic transition of frequency ω_0, from which the laser light is detuned by $\Delta = \omega_0 - \omega_l$. This equation is derived rigorously in [24]. For blue-detuned light, this potential is positive, resulting in a repulsive dipole force that pushes atoms towards regions of low intensity. Dipole traps are used in BECK for tight axial confinement of the BEC in z, and for radial confinement in $x-y$.

Radially, the trapping potential can be engineered using a digital micromirror device (DMD), most commonly used in video projectors. It consists of micrometer scale mirrors that can be switched on or off to shape the intensity profile of the dipole laser. Furthermore, the DMD mirror states can be rapidly updated, allowing for a dynamic arbitrarily shaped trapping dipole potential [25], which is a key parameter for analog quantum simulation.

1.1.2 Phase Imprinting

The DMD enables spatial phase imprinting on the quasi-2D BEC. In the mean field description, the BEC can be described by an effective wavefunction [26]

$$\psi(x, y, t) = \sqrt{n(x, y, t)} e^{i\phi(x,y,t)} \quad , \tag{1.3}$$

where $n(x, y, t)$ is the BEC density distribution. In thermal equilibrium,

$$\phi(x, y, t) = -\mu t \quad , \tag{1.4}$$

where the chemical potential μ is given in the Thomas-Fermi approximation by

$$\mu = n(x, y) g_{\text{2D}} + V(x, y) \quad , \tag{1.5}$$

where g_{2D} is the effective 2D interaction strength. For a constant potential V within the trapping region, a thermally equilibrated BEC is stationary, with a flat density and phase profile. By locally varying the potential by $U(x, y)$ for a sufficiently small duration Δt such that the density profile remains constant, the BEC is perturbed from equilibrium, accumulating a phase shift given by

$$\Delta\phi(x, y) = -U(x, y)\Delta t \quad . \tag{1.6}$$

This technique is used throughout Chapter 5 to generate velocity fields to be probed with Bragg scattering.

2. Bragg Scattering in Quantum Gases

Bragg scattering was initially observed in 1913 as a phenomenon in X-ray crystallography. X-rays would only scatter coherently from a crystal at specific incident angles θ, providing the first evidence of a periodic lattice structure. Building on this, Brillouin and Bloch interpreted the phenomenon as a reflection process [27, 28]. When the X-ray momentum along the lattice axis lies on a Brillouin zone boundary, a discrete momentum is transferred and the X-ray reflects. Varying θ changes this momentum component, allowing for the determination of the lattice spacing Λ by identifying Brillouin zone boundaries.

In the 1980s, this concept was applied to quantum gases. Here, the role of light and matter swap places: It was demonstrated that moving beams of atoms coherently scattered from static optical lattices with the same θ dependence [29–31]. Soon after, a configuration for Bragg scattering static ultracold atomic clouds was implemented. A moving optical lattice, formed by counterpropagating laser beams, is swept through a cloud of cold atoms. The speed of the moving lattice depends on the relative detuning of the counterpropagating beams δ. Varying δ changes the atomic momentum relative to the lattice. When an atom's momentum $\boldsymbol{q}_A$ corresponds to a relative momentum along the optical lattice axis coinciding with the Brillouin zone boundary, the atom absorbs momentum and scatter coherently from the cloud. Bragg scattering in crystallography is therefore related to this configuration of Bragg scattering in quantum gases by:

$$\begin{aligned} \text{Crystals} &\rightarrow \text{Quantum Gases} \\ \text{x-rays} &\rightarrow \text{atoms} \\ \text{crystal} &\rightarrow \text{light} \\ \text{scan } \theta \text{ to probe } \Lambda &\rightarrow \text{scan } \delta \text{ to probe } \boldsymbol{q}_A \end{aligned}$$

Bragg scattering with moving optical lattices was first demonstrated with laser-cooled atoms in 1994 [32], and was used 5 years later on quantum gases to coherently split a Bose-Einstein condensate [33]. In the present, Bragg scattering has since been used to spectroscopically probe low-energy phononic regimes in quantum gases, providing experimental benchmarks for theoretical models [34]. It has also found applications in atom interferometry as a coherent atomic beam splitter [35].

In this thesis, we develop the use of Bragg scattering to probe atomic velocities in quasi-2D BECs with spatial resolution. To gain a deeper understanding of the parameters and dynamics involved in Bragg scattering of quantum gases, we to analyse this system in a quantised photon picture, describing Bragg scattering as an inelastic, 2-photon atomic transition between momentum states. In this chapter we derive the velocity-dependent resonance of this transition, and describe the dependence of the transition linewidth on the duration and temporal shape of the Bragg pulse. Finally, we present 2 distinct velocimetric methods for spatially-resolved velocity field extraction.

2.1 2-photon Bragg Transitions

When two counterpropagating laser beams of frequencies ω and $\omega + \delta$ are incident on an atom, a 2-photon process can take place [36]. The higher energy photon is absorbed, exciting the atom to an intermediate 'virtual' state, and the lower energy photon simultaneously stimulates an emission, visualised in Fig. 2.1 (upper left). For a single photon detuning $\Delta = \omega - \omega_0$ much larger than Γ, the natural linewidth of $|g\rangle \rightarrow |e\rangle$, electronic excitation to $|e\rangle$ suppressed, and this 2-photon process dominates.

For $\delta \ll \omega$, the photon wavelengths are approximately the same: $\lambda_L(\omega) \approx \lambda_L(\omega+\delta)$. Through this process, the atom gains energy $\hbar\delta$ and momentum $+2\hbar\boldsymbol{k}_L$, $\boldsymbol{k}_L = 2\pi/\lambda_L\hat{\boldsymbol{x}}'$, where we define $\hat{\boldsymbol{x}}'$ as the Bragg beam axis [Fig. 2.1 upper left]. This inelastic process couples an initial atomic momentum state $|\boldsymbol{q}_A\rangle$ to a final state $|\boldsymbol{q}'_A\rangle$ with no modification of the electronic state, and is called a (first-order) Bragg transition [37].

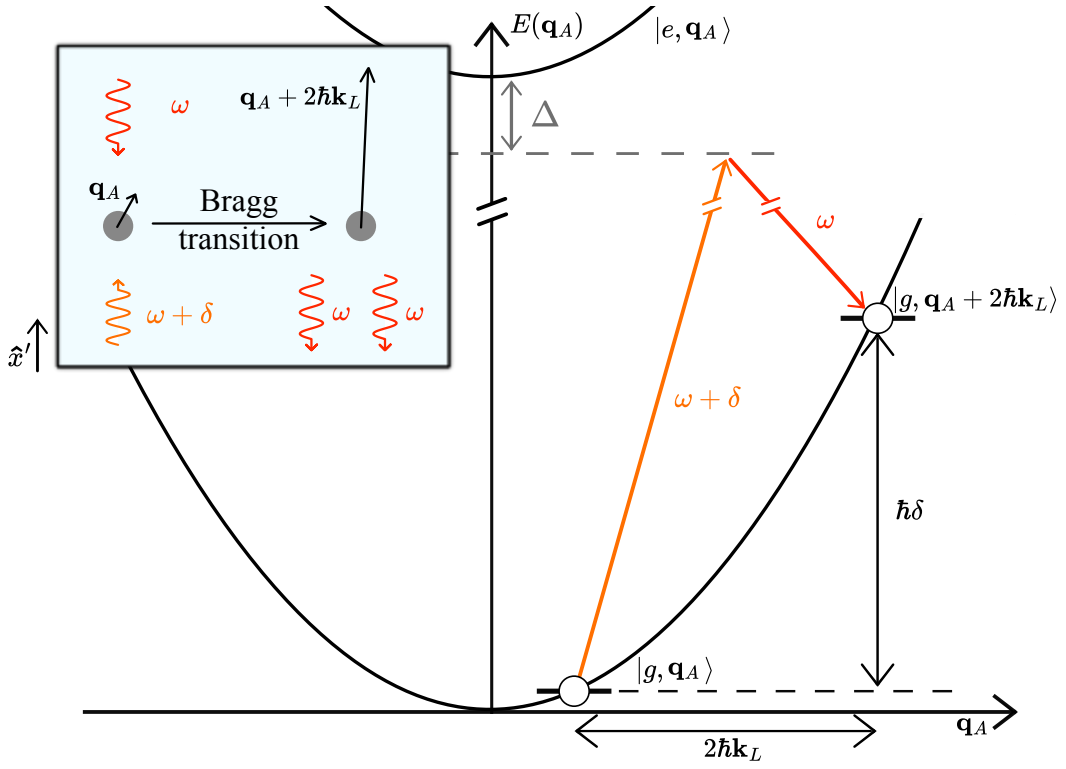

Figure 2.1: The Bragg transition. A diagram of the inelastic 2-photon Bragg transition from an initial atomic momentum state $|g, \boldsymbol{q}_A\rangle$ to a final state $|g, \boldsymbol{q}_A + 2\hbar\boldsymbol{k}_L\rangle$. The atom remains in the same electronic state $|g\rangle$ and gains energy $\hbar\delta$ and momentum corresponding to 2 photon recoil momenta due to the absorption and stimulated emission depicted in the upper left. The initial and final state are coupled by a 'virtual' intermediate state, which is detuned from the excited electronic state $|e\rangle$ by Δ. The resonance condition of this transition is found by enforcing conservation of energy and momentum such that the transition couples to an allowed energy given by the dispersion relation $E(\boldsymbol{q}_A)$.

The resonance condition for a Bragg transition is met when both energy and momentum are conserved:

$$\hbar\delta_{\text{res}} = E(\boldsymbol{q}'_A) - E(\boldsymbol{q}_A) \quad , \qquad (2.1)$$

$$\boldsymbol{q}'_A = \boldsymbol{q}_A + 2\hbar\boldsymbol{k}_L \quad . \qquad (2.2)$$

For a free atom of mass m with momentum $\boldsymbol{q_A}$, the dispersion relation $E(\boldsymbol{q}_A)$ is simply given by the kinetic energy $\frac{|\boldsymbol{q}_A|^2}{2m}$, and is plotted in Fig. 2.1. The Bragg resonance for this system is found at

$$\hbar\delta_{\text{res}} = \frac{|\boldsymbol{q}_A + 2\hbar\boldsymbol{k}_L|^2}{2m} - \frac{|\boldsymbol{q}_A|^2}{2m} \quad . \tag{2.3}$$

Expanding this, we find that the resonance depends linearly on the atomic velocity $\boldsymbol{v} = \boldsymbol{q}/m$

$$\delta_{\text{res}} = \frac{2\hbar|\boldsymbol{k}_L|^2}{m} + 2\boldsymbol{k}_L \cdot \boldsymbol{v} \quad . \tag{2.4}$$

The first term is the resonance for a stationary atom:

$$\delta_0 := \frac{2\hbar|\boldsymbol{k}_L|^2}{m} \quad . \tag{2.5}$$

For a 2-photon detuning $\delta = \delta_0$, we couple stationary atoms to a momentum of $2\hbar\boldsymbol{k}_L$. The second term introduces a dependence on the velocity of the interrogated atom. For an atom moving along the beam axis, the two photon frequencies appear blue- and red-detuned by $\pm\boldsymbol{k}_L \cdot \boldsymbol{v}$ respectively. This results in the relative photon detuning in the frame of the atom decreasing by $2\boldsymbol{k}_L \cdot \boldsymbol{v}$. We therefore define a Doppler detuning term in Eq. 2.4,

$$\delta_d(v_\parallel) := 2\boldsymbol{k}_L \cdot \boldsymbol{v} \quad , \tag{2.6}$$

which brings the system in the atom frame into resonance. We can therefore probe the velocity component along the beam axis $v_\parallel$ by scanning $\delta_d(v_\parallel)$ and measuring the atoms coupled into the final momentum state $|\boldsymbol{q}_A + 2\hbar\boldsymbol{k}_L\rangle$.

2.2 Effective 2-level System

The resonance condition described above captures coupling between two quantum mechanical states through an external oscillating field. Provided $\Delta \ll \Gamma$, such that the spontaneous scattering rate $\Gamma_{sc} \propto \frac{\Gamma}{\Delta^2}$ is suppressed, the time dynamics of the state occupations are captured by the standard treatment of a 2-level system characterised by the interaction

$$\hat{\boldsymbol{H}} = \frac{\Omega_R(t)}{2} e^{i\delta t} |\boldsymbol{q}_A\rangle \langle \boldsymbol{q}'_A| + h.c. \quad , \tag{2.7}$$

where the coupling strength depends on 2-photon Rabi frequency

$$\Omega_R(t) = \frac{\Omega(t)^2}{2\Delta} = \frac{I(t)}{\epsilon_0\hbar c} \frac{\langle g| \hat{\boldsymbol{\epsilon}} \cdot \hat{\boldsymbol{d}} |e\rangle}{\Delta} \quad , \tag{2.8}$$

where time dependence is introduced by the time-varying incident laser intensity $I(t)$, which modifies $\Omega(t)$, the electronic Rabi frequency coupling $|g\rangle$ and $|e\rangle$. To couple the 2 momentum states, the electronic transition's electric dipole matrix element $\langle g| \hat{\boldsymbol{\epsilon}} \cdot \hat{\boldsymbol{d}} |e\rangle$ must be non-0. Therefore $|g\rangle \rightarrow |e\rangle$ must be an *allowed* atomic dipole transition, for which the laser light should have the correct polarisation $\boldsymbol{\epsilon}$, an important consideration for the technical setup discussed in Chapter 3.

2.2.1 Rabi Oscillations and Spectral Response

To investigate the spectral and temporal behaviour of the Bragg transition, we analyse the system using the interaction Hamiltonian $\hat{\boldsymbol{H}}$ [Eq. (2.7)]. Treating $\hat{\boldsymbol{H}}$ as a weak perturbation, we apply first-order time-dependent perturbation theory, where the first-order final momentum state coefficient is given by [38]

$$c^{(1)}_{\boldsymbol{q}'_A} = c^{(1)}_{\boldsymbol{q}'_A}(0) - \frac{i}{\hbar}\int_0^t \langle \boldsymbol{q}'_A | \, \hat{\boldsymbol{H}} \, | \boldsymbol{q}_A \rangle \, e^{i\delta_{\text{res}} t'} \, dt' \quad . \tag{2.9}$$

In this framework, we find that the transition probability for an initial $|\boldsymbol{q}'_A\rangle$ population of 0 is given by

$$P_{\boldsymbol{q}_A \to \boldsymbol{q}'_A} \propto \left| \int_0^t \Omega_R(t') e^{i(\delta - \delta_{\text{res}})t'} dt' \right|^2 \quad . \tag{2.10}$$

This result reveals that the transition probability as a function of detuning from resonance, or the spectral lineshape, is proportional to the absolute square of the Fourier transform of the driving field $\Omega_R(t)$ as a function of time [39]. Therefore, the Bragg transition lineshape can be tailored through temporal shaping of the Bragg pulse, within experimental constraints.

In the case of a square pulse, the incident intensity and thus Ω_R is constant for some finite duration t_B. From Eq. 2.10 we can recover the familiar result discovered by Rabi in 1937 [40]:

$$P_{\boldsymbol{q}_A \to \boldsymbol{q}'_A} = \frac{\Omega_R^2}{\Omega_R^2 + (\delta - \delta_{\text{res}})^2} \sin^2\left(\frac{\sqrt{\Omega_R^2 + (\delta - \delta_{\text{res}})^2}}{2} t_B \right) \quad . \tag{2.11}$$

As t_B is scanned, the atomic state population oscillates coherently between the initial and final momentum states. On resonance, $\delta - \delta_{\text{res}} = 0$, this Rabi oscillation has a frequency Ω_R and amplitude 1. Here we define characteristic π pulse of duration $\Omega_{\text{eff}} T_\pi = \pi$, where atoms on resonance are coupled to the final momentum state with 100% probability.

As a function of δ, the spectral lineshape of the transition probability takes the form of a sinc^2 function centred around δ_{res}, equivalent to the absolute squared Fourier transform of the incident square pulse. This can be interpreted in two ways: first, the atoms interact not only with their resonant $\delta_d(v_\parallel)$ but also couple more weakly to other detunings. Alternatively, atoms exclusively interact with $\delta_d(v_\parallel)$, but the spectral peaks of the square pulse at ω and $\omega + \delta$ broaden due to the finite pulse duration Fourier limit. Therefore, a distribution of Doppler detunings are probed at the same time. In both pictures, this corresponds to a spectral broadening $\sim 1/T_B$, an important result when considering Bragg spectroscopy as a velocimetric tool.

2.3 Spatially-resolved velocimetry

Given its momentum-based coupling and velocity sensitive resonance, Bragg transitions are an excellent choice for atomic velocity imaging in BECs. Atoms of momentum state $|\boldsymbol{q}_A\rangle$ that are on resonance with a Bragg pulse gain momentum $2\hbar\boldsymbol{k}_L$ and scatter from the BEC. After a sufficiently large time of flight T_{TOF}, such that the scattered cloud separates spatially from the central BEC, the spatial distribution of both quasi-2D scattered and unscattered clouds can be recorded. For atomic momenta $\boldsymbol{q}_A \ll 2\hbar\boldsymbol{k}_L$, atoms do not move relative to each other during the time of flight, granting spatial resolution.

To perform spatial velocity field extraction, we discretise the velocity field into spatial bins $v(x_i, y_j)$. For each bin, the curvature of the phase field should be sufficiently small such that the bin has a well-defined velocity. With increased pulse durations, atoms experience prolonged interaction with external surroundings, introducing relative TOF dynamics.
Additionally, if larger atomic momenta are probed, relative TOF dynamics become dependent on the specific dynamics and interactions of the BEC. However, because the initial atomic momenta (along the beam axis) can be selected by via $\delta_d(v_\parallel)$ [Eq 2.4], this regime can be anticipated. Generally, the spatial resolution of the imaging system also sets a lower limit on the spatial resolution attainable.

When the BEC is probed with a Bragg pulse of 2-photon detuning δ and duration t_B, the spatially binned scattered distribution $n_{\text{scatt}}(x_i, y_j)$ and unscattered central distribution $n_c(x_i, y_j)$ can be compared to determine the spatial velocity field. Atoms in spatial bins with velocity components along the Bragg axis corresponding to $\delta_d = \delta - \delta_0$ scatter with maximum coupling efficiency. Due to spectral broadening, atoms from spatial bins of nearby velocities also scatter with lower transition probabilities, given by Eq.2.10. In the following, we define two distinct methods of spatially-resolved velocimetry. Their differences are illustrated in Fig. 2.2.

2.3.1 Spectroscopic Velocimetry

In this method, a reproducible quasi-2D BEC configuration is destructively probed by Bragg pulses of different δ in a *spectroscopic* fashion. For each spatial bin, the resonant $\delta_{\text{res}}(x_i, y_j)$ is found when atoms are maximally coupled to the scattered cloud. The spatial distribution of resonant Doppler detunings $\delta_d(x_i, y_j; v_\parallel)$ is then found using Eq. 2.4, from which the spatially-resolved 1D projected velocity field $v_\parallel(x_i, y_j)$ is found using Eq. 2.6. This is illustrated in Fig. 2.2 (upper right).

For spectroscopic velocimetry, the velocity range and resolution depend on the range and spacing of 2-photon detunings δ used to interrogate the BEC. The spectral broadening of the Bragg transition also impacts velocity resolution. A longer Bragg pulse duration, t_B results in a narrower spectral broadening, and thus spatial bins of velocities $v_\parallel$ and $v_\parallel + \Delta v_\parallel$ become easier to resolve for increasingly smaller $\Delta v_\parallel$.

Besides relative TOF dynamics, the spatial resolution of spectroscopic velocimetry is strongly influenced by the reproducibility of the BEC configuration. The less deterministic the BEC configuration, the larger the spatial bin of the extracted velocity field must be such that each bin still has a well-defined velocity.

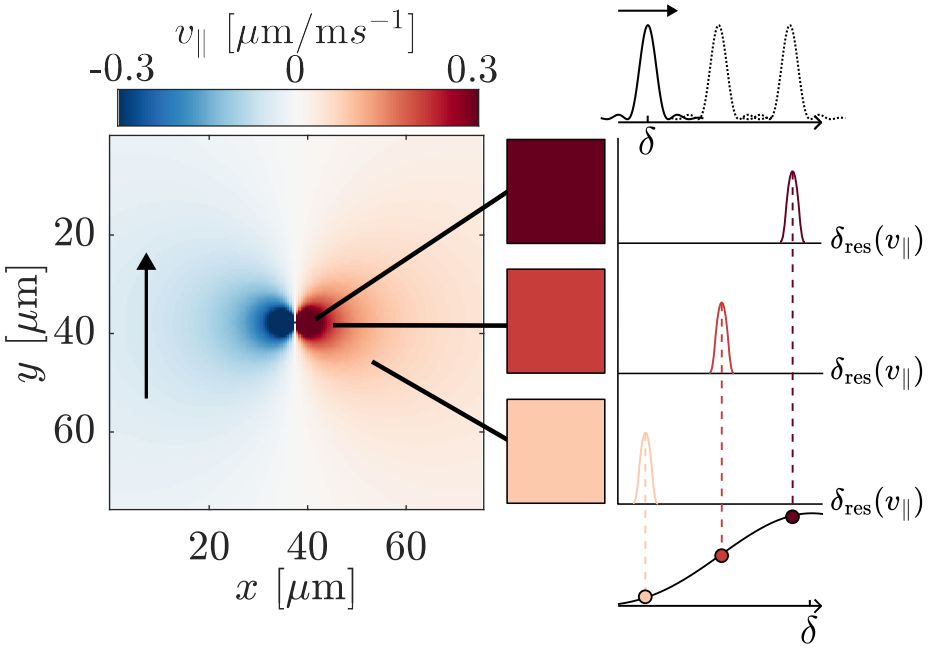

Figure 2.2: Illustration of the spectroscopic and broadband velocimetric methods. An example theoretical velocity field of a single vortex projected along the y axis is plotted (left). The spectral lineshapes of Bragg pulses centred around δ used in spectroscopic and broadband velocimetry are shown in the upper and lower right respectively. For the spectroscopic method, δ is scanned, and a spatial bin is maximally scattered $\delta = \delta_{\rm res}(v_\parallel)$. For the broadband method, the normalised scattered fraction is compared to lineshape centred around δ to determine $\delta_{\rm res}(v_\parallel)$.

2.3.2 Broadband Velocimetry

In *broadband* velocimetry, the BEC is probed with a Bragg pulse of shorter duration t_B such that the spectral broadening of the transition spans a range of $\delta_d(v_\parallel)$ resonant to atoms in the system. The normalised scattered fraction at each spatial bin, $n_{\rm scatt}(x_i, y_j)/n_c(x_i, y_j)$ gives a spatially-resolved transition probability $P_{\boldsymbol{q}_A \to \boldsymbol{q}'_A}(x_i, y_j)$, illustrated in Fig. 2.2 (lower right). The dependence of the transition probability on $\delta_{\rm res}$ is given by Eq. 2.10, or can be experimentally characterised [Section 4.3]. Since this response is symmetric about δ, the inverse of this function can be used to determine 2 possible values of $\delta_d(x_i, y_j)$ for each spatial bin, however the experimental implementation allows for one to be discarded [Section 5.2.2]. The spatially-resolved 1D projected velocity field $v_\parallel(x_i, y_j)$ is then found using Eq. 2.6.

Velocity resolution of broadband velocimetry depends on the range of velocities being probed. For a larger range, a broader spectral lineshape is required. This decreases the difference in normalised scattered fraction for velocities $v_\parallel$ and $v_\parallel + \Delta v_\parallel$, thus decreasing sensitivity. Ultimately, this is limited by how well the imaging system can resolve the atom number at a given position, which is technically challenging.

The key advantage of broadband velocimetry is the ability to extract spatially-resolved velocity fields in a single shot, enabling velocity field measurement for irreproducible turbulent systems. For deterministic, reproducible BEC configurations, spectroscopic velocimetry offers a higher velocity resolution. In Chapter 5, both methods are used to extract spatially-resolved velocity fields for vortex-antivortex systems using the experimental setup detailed in the next chapter.

3. Experimental Implementation

In this chapter, we first put numbers to the Bragg pulse parameters defined in Chapter 2, and outline the realisation of the counterpropagating, relatively-detuned laser light. We then describe the optical and electronic setup for Bragg scattering along 2 axes for 2D velocity field extraction and analyse the stability of generated Bragg pulses. Finally laying out the chronological protocol used to perform Bragg scattering experiments.

3.1 Realising the Bragg Beam

To excite a Bragg transition, atoms are illuminated with laser light with counterpropagating frequency components ω and $\omega + \delta$, where ω is detuned from the nearest electronic transition by $\omega_0 - \omega = \Delta$. The BEC is prepared with atoms in the ${}^2P_{1/2}$ state, and we choose to be red-detuned from the D1 transition (${}^2P_{1/2} - {}^2S_{1/2}$) with natural frequency $\omega_0 = 2\pi \times 389.286\,\text{THz}$ at zero magnetic field [41]. The D1 line is the lowest energy electronic transition from the ${}^2P_{1/2}$ state. Therefore, Δ can be large without the 2-photon transition coupling to a closer intermediate virtual state. To reduce heating via spontaneous emission Δ should be maximised [Section 2.1]. However, this reduces the 2-photon Rabi frequency Ω_R, given by Eq. 2.8. To compensate for this, the incident beam intensity can be increased accordingly. The maximum beam power in our setup is limited to $300\,\text{mW}$. These two parameters should be set such that $\Omega_R \sim 1\,\text{kHz}$. This value is selected to give a T_π duration ranging from $100\,\mu s - 1\,\text{ms}$, which is restricted based on spectral broadening and velocity field extraction spatial resolution, as discussed in Chapter 2. Under these constraints, $\Delta \sim 500\,\text{GHz}$ is found to be optimal, which corresponds to a laser wavelength of $\lambda_L \approx 771\,\text{nm}$.

To generate a mixed-frequency *counterpropagating* beam across the BEC in the lab, we first generate a *co-propagating* mixed frequency beam via amplitude modulation. Since

$$A\sin(\omega t)\sin(\delta t) \equiv \frac{A}{2}\left[\cos(\omega - \delta) + \cos(\omega + \delta)\right] \quad , \tag{3.1}$$

modulating the amplitude by a beat frequency δ resulting in *co-propagating* spectral components relatively detuned by δ. Experimentally, this is achieved using a single pass acousto-optic modulator (AOM) setup. From Eq. 2.5, $\delta_0 = 2\pi \times 34.2\,\text{kHz}$. From theoretical models of quantised vortices in quasi-2D BECs, we expect maximum velocities in regions of non-0 atomic density $\sim 1\,\mu\text{m/ms}^{-1}$, corresponding to a maximum Doppler detuning $\delta_d \sim 3\,\text{kHz}$. Therefore, we design the setup to generate detunings varying from $30 - 40\,\text{kHz}$.

To achieve counterpropagating photons illustrated in Fig. 2.1 (upper left), the laser beam is retroreflected [Fig. 3.1b], producing 2 sets of relatively detuned lasers capable of Bragg scattering. For a given detuning δ, atoms travelling in one direction along the beam axis with velocity corresponding to $\delta_d(v_\parallel) = \delta - \delta_0$ are resonantly coupled and recoil with $+2\hbar\boldsymbol{k}_L$ from the BEC. Simultaneously, atoms travelling with the opposite velocity corresponding to $-\delta_d$ are also in resonance with the *retroreflected* Bragg pulse, gaining $-2\hbar\boldsymbol{k}_L$ and recoiling in the opposite direction. This not only realises counterpropagating relatively-detuned photons needed for Bragg transitions, but also probes two velocity classes at once, a useful result for broadband velocimetry, discussed further in Section 5.2.2. For a stationary BEC, the

two directions are degenerate, and atoms couple to each final momentum state with equal probability, analogous to an *atomic* beam splitter.

3.2 Technical Setup

The setup for generating two *co-propagating* mixed-frequency laser pulses is shown in Fig. 3.1a. Laser light from a *Coherent MBR-110* Ti:Sa laser seeded by a *Coherent Verdi V10* 532 nm laser operating at 27 A is amplitude-modulated in two AOM paths. Beams from the two paths are then coupled individually to the experimental table to interrogate the BEC along 2 axes as illustrated in Fig. 3.1b.

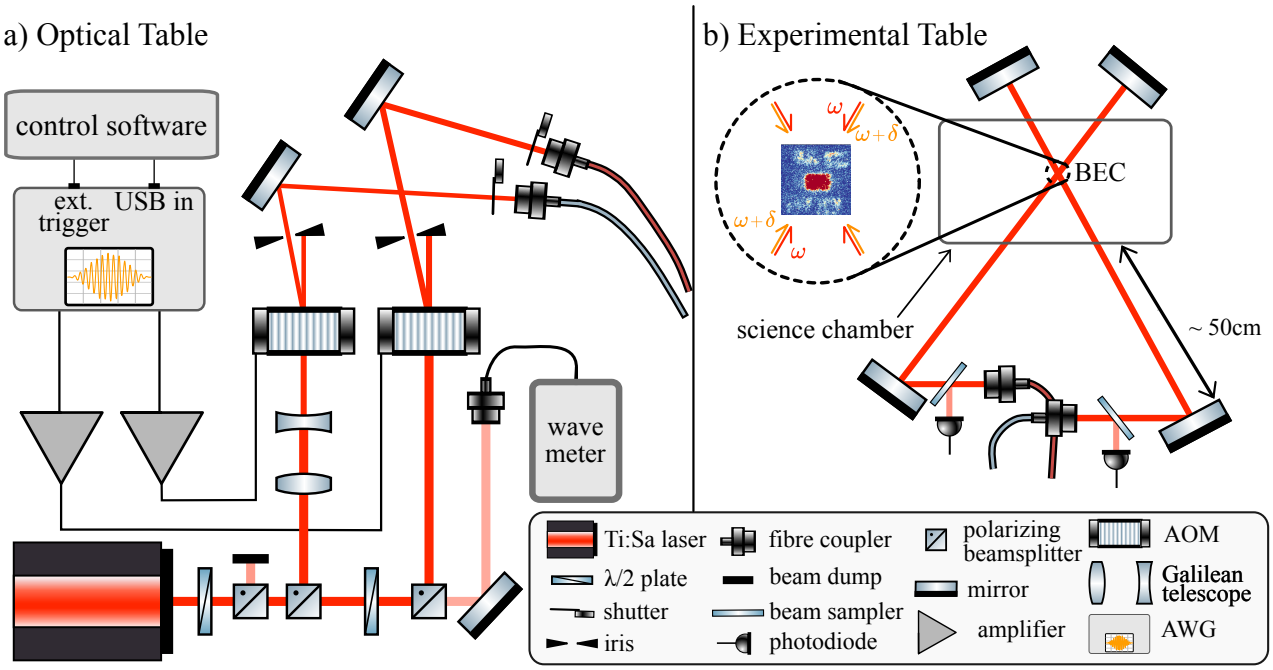

Figure 3.1: Experimental Bragg scattering setup. a) On the optical table, the majority of light is distributed amongst two AOM paths to produce individual co-propagating mixed-frequency pulses. A small amount of light is coupled into a wavemeter. The galilean telescope has 1.5x demagnification and is used for beam waist adjustment to suite the AOM numerical aperture. Irises are used to block the zero-order diffraction from the AOM. Shutters are implemented to prevent any unwanted light being coupled to the experimental table [42]. The AOM signals are generated in the control software and applied to the AOMs with an arbitrary waveform generator (AWG) via 34 dB 24 V amplifiers. **b)** Bragg pulses are coupled to the experimental table. A beam sampler is used to measure beam powers for power stabilisation. The beams are retroreflected across the BEC in a vacuum chamber, forming retroreflected Bragg pulses which probe velocities along two axes at a relative angle of 47°.

The Ti:Sa's tuneable frequency range allows for the single photon detuning Δ to be tuned and optimised. At $\lambda_L \sim 771$ nm, the Ti:Sa outputs approximately 700 mW of vertically polarised light. Throughout the setup, $\lambda/2$ plates and polarising beam splitters are used to select the beam power distributed amongst two AOM paths and a small amount ($< 1\%$) is coupled into a fibre-based High Finesse WS6 Wavemeter to monitor the laser frequency. Note that each AOM path is used to generate an independent amplitude-modulated Bragg beam. These can

be used to probe the atomic velocities along two directions, allowing for the extraction of information on the full vector velocity field, demonstrated in Section 5.3.

Amplitude Modulation

The AOM couples the incident beam into multiple diffraction orders. The nth order beam is detuned from the incident beam by $n\Omega_{\text{AOM}}$, where Ω_{AOM} is the radio frequency of the AOM driving signal. For each AOM path, the angle of incidence is adjusted to maximise the first-order diffraction efficiency, defined as the ratio of first-order power with respect to the input beam power. Since $\Delta \gg \Omega_{AOM}$, the additional detuning introduced to the first-order beam has a negligible effect on the Rabi frequency [Eq 2.8]. We employ AOMs of different Ω_{AOM} ($110\,$MHz and $80\,$MHz) in each beam path to avoid interference effects between the two Bragg axes.

So far, the Bragg beams are monochromatic. Co-propagating mixed-frequency components are generated via amplitude modulation by a beat frequency δ. The AOM signal contains Ω_{AOM}, δ, and an arbitrary time-varying envelope $A(t)$ to define the pulse shape:

$$V(t) = A(t)\sin^2\left(\frac{\delta}{2}t\right)\sin\left(\Omega_{\text{AOM}}t\right) \quad . \tag{3.2}$$

The signal is generated as a 1D array in the control software with a sampling rate of $1\,$MHz, corresponding to the maximum sample rate of the *Keysight 33600A* arbitrary waveform generator (AWG). The array is uploaded to the AWG, which is set to trigger on a $5\,$V TTL signal. Upon triggering, the AWG outputs the signals to the AOMs via $34\,$dB amplifiers, and the 2 independent mixed-frequency Bragg beams are pulsed on with the desired pulseshape.

Cold Coupling and Hitting the Atoms

Each Bragg beam is coupled to the experimental table via a $10\,$m single-mode polarisation-maintaining optical fibre using a cold-couple method. The AOM is pulsed on for $50\,\mu$s at $2\,$kHz whilst optimising the coupling efficiency to $\sim 60\%$. This avoids coupling the fibre to a deviated mode due to laser-induced heating. On the experimental table [Fig. 3.1b], the beams are out-coupled with horizontal polarisation such that they address the D1 transition. After collimation by the fibre out-coupler, they reflected off a mirror towards the science chamber. This arrangement allows for sufficient degrees of freedom to finely adjust both the beam position and Poynting.

To align a Bragg beam with the atomic cloud, we begin with visual alignment with the coplanar 3D MOT beams, which are positioned nearby and responsible for preliminary stages of cooling and trapping the atoms. Next, we tune the laser frequency to resonance with the D1 transition. We pulse the beam while the BEC is present in the dipole trap and reduce the beam power until the atoms are no longer scattered away due to heating from spontaneous emission. Then we tune the beam by adjusting the fibre and mirror mount to re-maximise atom loss. Once optimised in an iterative manner, the Bragg beam and BEC intersect along the beam axis. A retroreflecting mirror on the other side of the science chamber is first aligned visually such that the ingoing and reflected beams pass through a small iris, after which fine adjustment is carried out by maximising the amount of light that couples back into the fibre. This ensures proper alignment of the retroreflected beam relative to the ingoing beam, and realising the counterpropagating beam setup required for Bragg transitions.

3.2.1 Bragg Pulse Stability

Bragg scattering for spatially-resolved velocimetry requires stable, reproducible Bragg pulse parameters. Any error or fluctuation impacts the Rabi oscillation via Eq. 2.11, increasing the uncertainty in the fraction of atoms scattered for a given parameter set. The Bragg pulse parameters fall into two groups: single photon detuning Δ and beam intensity I governed by Ti:Sa stability, and 2-photon detuning δ, envelope shape $A(t)$, and pulse duration T_B which depend on the AOM and AWG.

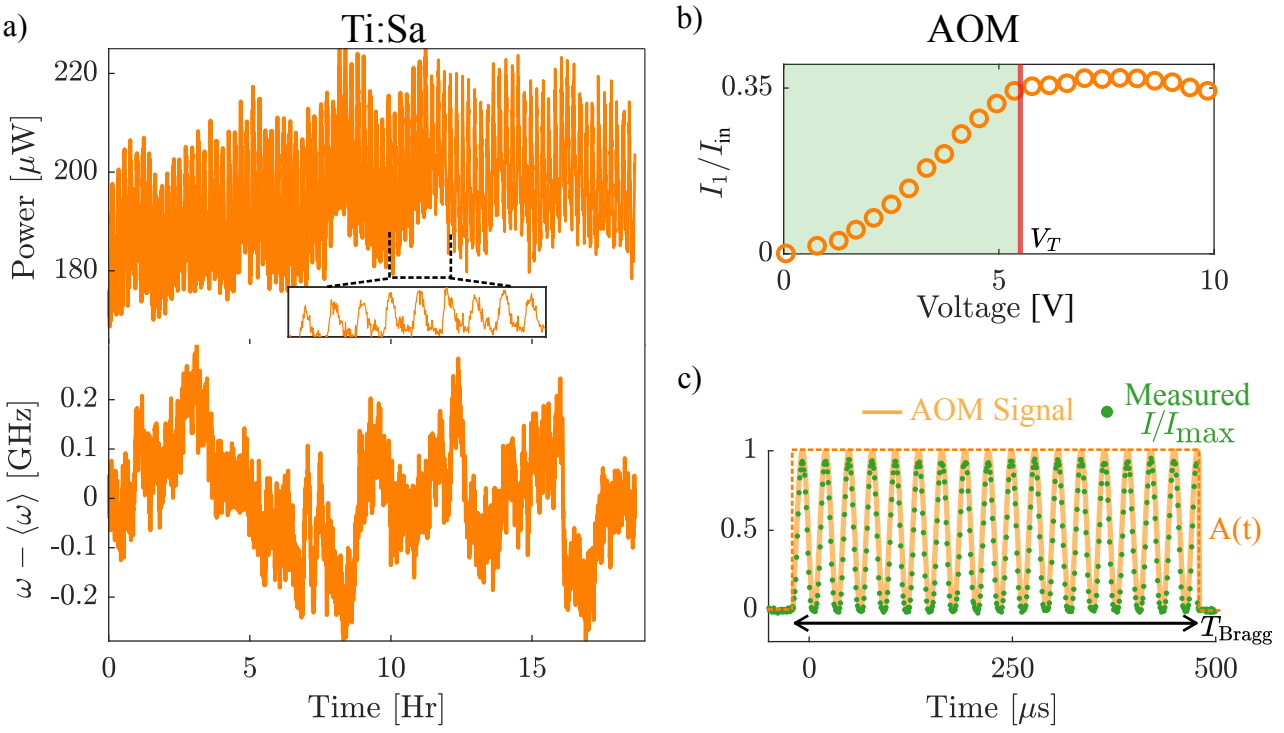

Figure 3.2: Measuring stability and reproducibility of Bragg pulses. a) Ti:Sa output frequency ω and power (after a beam sampler) stability taken using a HighFinesse WS6 wavemeter over several hours. Frequency fluctuations (lower) about the mean value, $\langle\omega\rangle = 389.083\,\text{THz}$ have a standard deviation $\sigma_\omega = 106\,\text{MHz}$. The output Ti:Sa power fluctuates periodically with amplitude $\pm 10\%$ and a period of about 15 minutes. **b)** AOM response curve recorded by scanning the input AOM driving signal amplitude $0 - 10\,\text{V}$ while measuring the first-order beam intensity I_1 with a fast photodiode, plotted relative to the input beam intensity I_{in}. This response is approximately linear until a threshold voltage, $V_T = 5.6\,\text{V}$. The second AOM has a similar response shape, with $V_T = 1.1\,\text{V}$ and a max. $I_1/I_{\text{in}} = 0.9$. **c)** An example of the Bragg pulse AOM signal and square envelope $A(t)$ (orange) and first-order beam intensity (green) measured with a fast photodiode.

During Bragg scattering experiments, we occasionally observed the scattered fraction suddenly fall to 0 for all δ due to mode hopping of $200\,\text{GHz}$ in the Ti:Sa laser. After realignment and calibration of the internal etalon and cavity locks, the frequency is stabilised and drifts negligibly compared to Δ, demonstrated in Fig. 3.2 (lower). Ti:Sa output power measurements, plotted in Fig. 3.2 (upper), show fluctuations of approximately $\pm 10\%$ with a period of around 15 minutes, likely due to periodic temperature fluctuation in the Ti:Sa cooling water with a period of around 30 minutes. The power fluctuation is the largest source of uncertainty in the Bragg scattering setup, and can be reduced by implementing sample and hold PID power stabilisation, which was not implemented in this work. For 2-photon Rabi frequency $\Omega_R = 2\pi \times 1\,\text{kHz}$, this results in a maximum atom number fluctuation of 7.8% at $t_B = T_\pi/2$.

For amplitude modulation, we assume the response of the AOM to be linear with input

voltage. The measured response, plotted in Fig. 3.2b, is found to be approximately linear until some threshold voltage V_T. The deviation from a linear response at low V has a negligible effect on the Bragg beam spectrum. Fig. 3.2c shows the normalised input AOM signal and the corresponding measured first-order beam intensity I_1. To evaluate reproducibility, we measure I_1 for 20 consecutive pulses over 5 minutes and extract the phase, frequency, amplitude, and duration by fitting Eq. 3.2. All parameters are found to vary negligibly ($< 0.1\%$) shot to shot.

3.3 Experimental Sequence

With a technical setup capable of generating stable and reproducible Bragg pulses, we layout the experimental sequence for Bragg scattering experiments. Digital control is achieved through the remote control of the AWG. On every measurement there are fluctuations that arise both in the density and velocity profiles due to both quantum noise and fluctuations in the experimental setup. Therefore, it is useful to repeat measurements for the same parameter set to build up a mean picture.

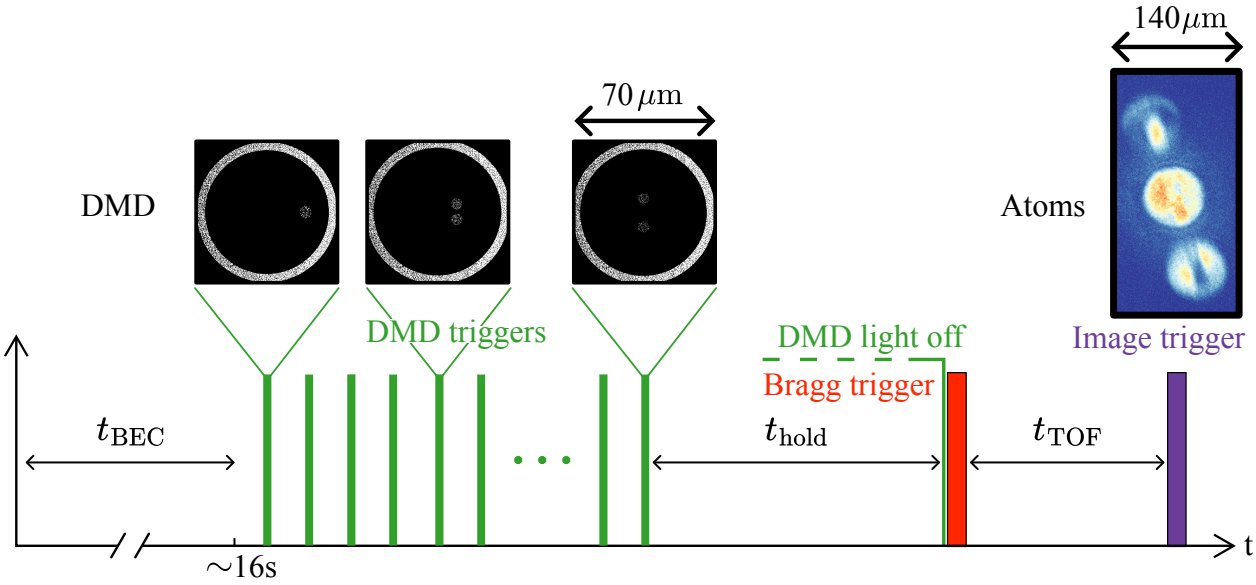

Figure 3.3: Chronological sequence of events for Bragg scattering experiments. The duration of a shot is approximately 16 s, where the majority of that duration t_{BEC} is spent producing the condensate. Afterwards, a series of TTL signals can be sent to the DMD, triggering it to move to the next image in an uploaded folder. Like a flipbook, the DMD goes through the images producing a time-varying trapping potential. After duration t_{hold} on the order of milliseconds, the DMD light is shut off, and the Bragg pulse is triggered immediately after. After a time of flight t_{TOF}, a final signal triggers an image to be recorded. Above the timeline, example DMD images show the radial trap, and chopstick method [Section 5.2.1]. White pixels correspond to mirrors turned on. The resulting atom image shown is averaged over 12 realisations. Note that the initial DMD loading sequence and final chopstick ramp down are not shown.

The Bragg scattering experimental sequence is as follows: A script defines the parameter set for each shot and number of repetitions per parameter set. For each shot, an interpreter compiles a time sequence of analog signals and digital triggers from the given parameter set. At the start of the sequence, the script uploads the AOM signal defining the Bragg pulse parameters to the AWG. During the first $\sim$ 16 s, atoms are trapped, cooled, and condensed, producing a quasi-2D condensate with a density profile determined by the radial dipole trapping potential, which is painted with the Digital Micromirror Device (DMD). From this

stage, the trapping potential can be varied in time to achieve certain dynamics in the BEC, as used in Chapter 5 to generate out-of-equilibrium configurations. After a variable hold time, a $5\,\mathrm{V}$ TTL signal triggers the AWG, and the BEC is probed with a Bragg pulse. After a time of flight, where the DMD trap is turned off, and the scattering length is kept the same, the spatial distribution of atoms is measured with absorption imaging [43]. This timeline is visualised in Fig. 3.3. With the technical setup and experimental sequence in place, we can start to investigate Bragg scattering experimentally by probing stationary BECs in the next chapter, and more dynamical, out-of-equilibrium configurations in Chapter 5.

4. Characterising Bragg Scattering in Stationary Bose-Einstein Condensates

Before employing Bragg scattering for velocity field extraction, we characterise the response of a stationary BEC to a Bragg pulse along a single axis. The stationary BEC has a flat phase gradient, and therefore negligible velocity broadening compared to the Bragg transition spectral broadening [Section 2.2.1]. The retroflected Bragg pulse setup described in Chapter 3 is expected to evenly scatter the condensate in $\pm 2\hbar \boldsymbol{k}_L$, with a resonant 2-photon detuning $\delta = \delta_0$. These measurements serve to characterise the system and establish parameters that optimise resolution and accuracy in subsequent velocity field measurements. First, we discuss the data extraction method. Then, we explore how the BEC reacts to interrogation from Bragg pulses of varying duration T_B and 2-photon detuning δ.

4.1 Experimental Protocol and Data Extraction

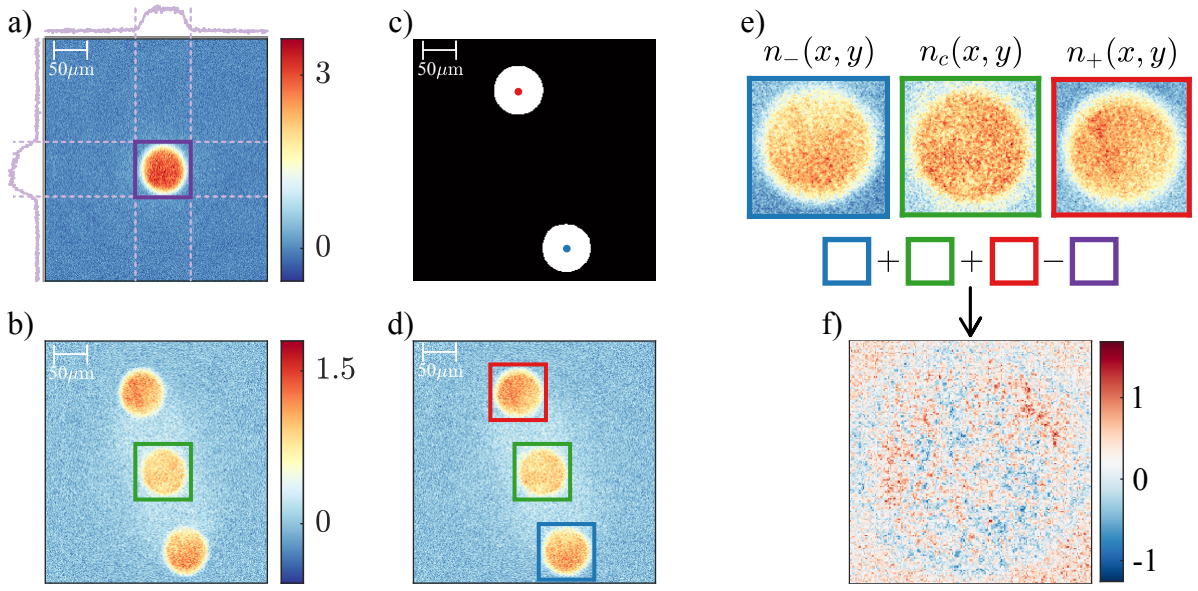

Figure 4.1: Extraction of scattered and unscattered cloud spatial atom distributions. a) Reference density distribution with no Bragg scattering to locate the central unscattered cloud. The cloud diameter is extracted from the density lineout in both axes, plotted in purple. The colorbar shows atoms per pixel. **b)** Scattered image after a Bragg pulse with the central cloud region found from a). In this example, $T_{\mathrm{TOF}} = 5\,\mathrm{ms}$. **c)** Binary mask where the atom per pixel signal exceeds a set threshold and the central cloud is masked out. Before applying the threshold, a Gaussian blur is applied to improve signal to noise. **d)** Resulting extracted regions. **e)** Extracted density distributions. **f)** The extracted distributions are summed and the reference distribution is subtracted to verify no offset between extracted distributions. Colorbars indicate atoms per pixel.

Following a manual calibration to find T_π, the BEC is interrogated by a single Bragg pulse, coupling atoms in opposite directions along the Bragg axis [Fig. 4.1b]. Each shot yields a spatial density distribution of atoms per pixel, which is processed to extract the spatial atom distributions of the unscattered (central) cloud, $n_c(x, y)$, and the two scattered clouds

$n_+(x, y)$ and $n_-(x, y)$, which should be symmetric for a stationary condensate. For velocity field reconstruction, it is critical to accurately locate the three clouds, such that corresponding spatial bins can be overlapped. This process is visualised in Fig. 4.1.

First, a reference image [Fig. 4.1a] without Bragg scattering is used to define the central cloud diameter and centre via a Gaussian fit in both axes. Then, the central cloud is occluded from the shot image [Fig. 4.1b], and the scattered cloud positions are found by applying a binary mask to isolate regions of high density, and calculating the centre of mass in the upper and lower halves of the image [Fig. 4.1c]. Assuming that scattered atoms do not move relative to each other during the TOF, the scattered clouds should have a maximal radius equal to the central cloud. Therefore, square masks of a fixed size slightly larger than the central cloud diameter and centred around the upper and lower centre of masses are used to extract n_+ and n_-. Examples of the extracted distributions are shown in Fig. 4.1d. Alignment is verified by finding the residual between the summed extracted distributions and the reference image. Shown in Fig. 4.1e, the residual within the cloud fluctuates with typical shot-to-shot fluctuations, while a positive signal outside of the cloud indicates spontaneous heating induced by the Bragg pulse.

The total number of atoms in each cloud is computed as the pixel-wise sum:

$$N = \sum_i \sum_j n(x_i, y_j) \quad , \tag{4.1}$$

and the total scattered fraction is defined as

$$n_{\text{scatt}} = \frac{N_+ + N_-}{N_T} \quad , \tag{4.2}$$

where N_T is the total number of atoms given by

$$N_T = N_+ + N_- + N_c \tag{4.3}$$

This method is applied either to extract $n_\pm(x, y)$ for individual shots, or for images averaged over multiple repetitions to average out shot-to-shot noise. When averaging over shots, the shot-to-shot standard deviation in atom number can also be calculated to provide a measure of stability.

4.2 Rabi Oscillations Between Momentum States

To investigate the coherence of population transfer between momentum states, we vary the Bragg pulse duration t_B at the fixed 2-photon detuning δ_0 to couple to stationary atoms. Note that δ_0 is found experimentally and differs slightly from the theoretical prediction from Eq. 2.5, discussed further in the next section.

The scan of t_B is repeated for two different Bragg beam intensities, corresponding to different 2-photon Rabi frequencies Ω_R. The scattered atom fraction is plotted against t_B with the corresponding atom images in Fig. 4.2, revealing Rabi oscillation expected from theory outlined in Chapter 2.

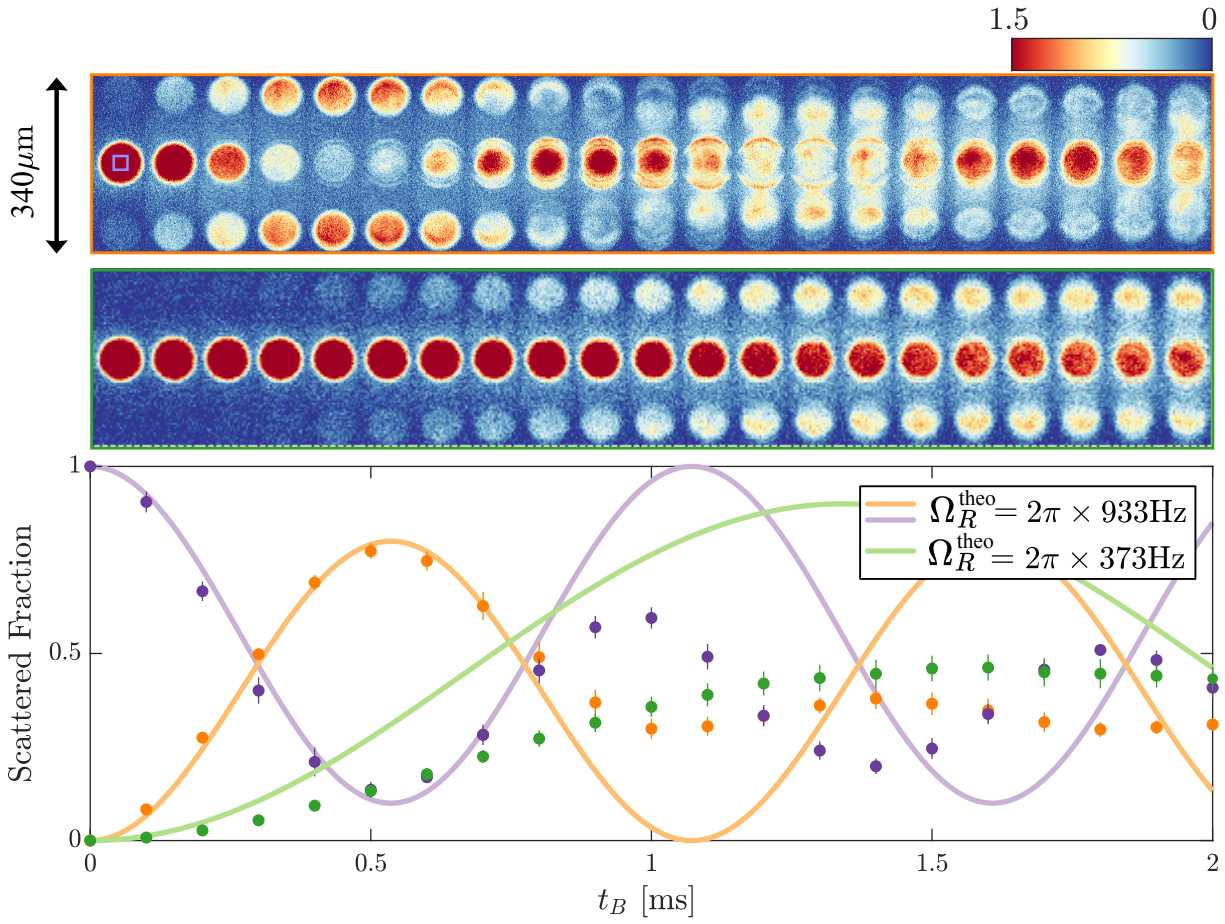

Figure 4.2: Rabi oscillations between momentum states. Experimental results for Bragg scattering with a square pulse of increasing duration, t_B. The orange and green points show the scattered fraction of atoms corresponding to the upper and lower rows of images, respectively. The colorbar indicates atoms per pixel. For each row, the incident Bragg pulse power is different, resulting in different Rabi frequencies. The solid lines show theoretical Rabi oscillations, with amplitudes scaled to twice the average value after damping. The relative number of atoms at the centre of the unscattered clouds is also plotted in purple for $\Omega_R^{\text{theo}} = 2\pi \times 933\,\text{Hz}$. The images are averaged over 12 shots. Error bars represent the shot-to-shot standard deviation.

For both intensities, the corresponding theoretical Ω_R^{theo} is calculated using Eq. 2.8 and plotted with solid lines in Fig. 4.2. For $\Omega_R^{\text{theo}} = 2\pi \times 933\,\text{Hz}$ at pulse durations $t_B < 500\,\mu$s, measured data agrees well with the expected oscillatory behaviour [Section 2.2.1]. However, the maximum observed scattered fractions are less than 1. For longer pulse durations the system exhibits damping, and decays to half the oscillation amplitude. Both effects originate from a broadening in the BEC momentum distribution due to the finite temperature of the condensate, and because the atoms are Bragg scattered after being released from the trap and expand ballistically. Atoms on the edge have the highest potential energy, and thus expand outwards the fastest. This leads to a spread in resonant detunings, $\delta_{\text{res}}(v_\parallel)$ which are a function of the component of atomic velocity along the beam axis. Consequently, atoms oscillate between the momentum states with a range of effective Rabi frequencies [Eq. 2.11]

$$\Omega_{\text{eff}} = \sqrt{\Omega_R^2 + (\delta - \delta_{\text{res}}(v_\parallel))^2} \quad . \tag{4.4}$$

This broadening causes dephasing of the coherent dynamics, and is the same effect that underpins velocity field imaging. Dephasing is largest for the faster atoms at the edge, where for $t_B = 700\,\mu$s they are in antiphase with the atoms closer to the centre. We also plot the

number of atoms inside a smaller area at the centre of the cloud, shown by the purple box in Fig. 4.2. The resulting oscillation is longer sustained since the spread of atomic momenta in this region is lower; however, dephasing still occurs. The dephasing happens on a shorter timescale for $\Omega_R^{\text{theo}} = 2\pi \times 343\,\text{Hz}$, where Ω_{eff} is smaller and thus more sensitive to changes in $\delta_{\text{res}}(v_\parallel)$. Here, the system is heavily damped, and does not perform any oscillation, as seen in Fig. 4.2. Additionally, for both Ω_R, the centre of mass of the scattered clouds decreases for longer t_B due to interactions with the background magnetic potential harmonic trap. This potential induces a force on the atoms during the Bragg interaction, smearing their final positions and reducing spatial resolution.

4.3 Spectral Response

The spectral response of the BEC can be measured by scanning the 2-photon detuning δ of incident Bragg pulses. As discussed in Section 2.2, the Bragg transition lineshape is directly proportional to the absolute square of the Fourier transform of $\Omega_R(t)$, which inherits time dependence due to a time-varying laser intensity defined by a pulseshape $A(t)$, varying between 0 and 1. With the setup described in Chapter 3, we can generate arbitrary positive-valued pulse shapes through which we engineer the shape of the spectral response. More complex pulseshapes with negative $A(t)$ have been demonstrated in modified setups using a π phase shift [39]. The transition lineshape for a given atom of arbitrary velocity $\boldsymbol{v}$ is centred around $\delta_{\text{res}}(v_\parallel)$, where $v_\parallel$ is the component of velocity along the Bragg beam axis. Therefore, the total spectral response of the BEC is a convolution of the transition lineshape with the atomic velocity distribution. For stationary condensate, velocities are narrowly broadened about 0. Thus, by scanning δ we expect to recover the transition lineshape centred around δ_0.

This response critically influences the velocity field extraction techniques employed in Chapter 5. The narrow spectral broadening optimal for *spectroscopic* velocimetry is achieved through a square pulse. The corresponding sinc^2 response function is not ideal for *broadband* velocimetry, where side lobes decrease the ability to map the number of scattered atoms to a corresponding velocity. In this case, a Hann pulseshape is more suitable [44].

4.3.1 The Hann Window

The Hann pulse, more commonly referred to in audio processing as the Hann window, is a raised cosine defined as:

$$A(t) = \cos^2\left(\frac{\pi t}{T_{\text{H}}}\right) \quad . \tag{4.5}$$

From Eq.2.10, a π pulse occurs when the integral of the absolute squared Fourier transform is $1/2$. For a Hann pulse, this requires a duration $T_{\text{H}} = 2t_B$, where t_B is defined as the duration of the square Bragg pulse. For this scaling, both pulseshapes achieve a π pulse at $t_B = T_\pi$. The Hann and square lineshapes are plotted in Fig. 4.3a.

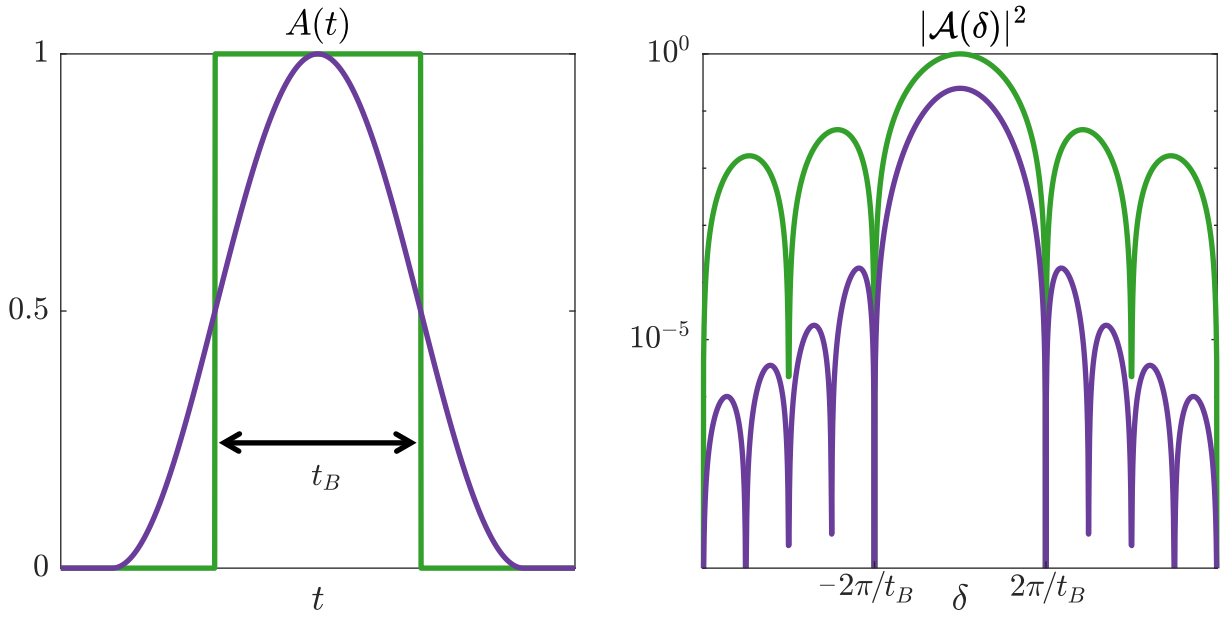

Figure 4.3: Hann and square pulseshapes and frequency spectra. The temporal Hann (purple) and square (green) pulseshapes (left). For a given square pulse duration t_B, the total Hann pulse duration is $T_H = 2t_B$ for the same spectral power. Bode plot spectra are centred around the 2-photon Bragg pulse detuning δ (right). Both mainlobes have width $4\pi/t_B$, and the sidelobes of the Hann pulseshape are strongly suppressed.

Unlike the square pulse, the Hann pulse has a continuous first derivative, which strongly suppresses spectral sidebands. For a square pulse, the first sidelobe drops to $-13\,$dB, whereas for the Hann pulse it is suppressed to $-31.5\,$dB. This suppression comes at the cost of a broader central lobe for a given t_B [45]. The absolute squared Fourier transforms of the pulseshapes are analytical and compared in Fig. 4.3b. The square pulse spectral response is given by Eq. 2.11, and the Fourier transform of the Hann lineshape $\mathrm{A}(\delta)$ is given by

$$\mathcal{A}(\delta) = \frac{\pi^2 \sin(t_B\delta/2)}{L\delta\,(\pi^2 - t_B^2\delta^2)} \quad . \tag{4.6}$$

Therefore, the Hann pulse is an ideal candidate for *broadband velocimetry*, for which sideband suppression is a priority, and a very narrow response is not required.

4.3.2 Experimental Results

We investigate the spectral response of a BEC at equilibrium to both square and Hann pulses by scanning δ from $30 - 40\,$kHz, around the expected Bragg resonance for stationary atoms $\delta_0 = 34.2\,$kHz [Eq. 2.5]. At each detuning, n_{scatt} is extracted using the image analysis method discussed in Section 4.1. Results are shown in Fig. 4.4 for $t_B = 300\,\mu$s and $500\,\mu$s.

Each spectral response profile is compared to theoretical predictions for the transition lineshapes from Eqs. 2.11 and 4.6. To fit the solid lines, amplitude and central detuning δ_0 are free parameters, while the spectral broadening is fixed by t_B. As expected, square pulses reveal clear sidelobes consistent with theory, while Hann pulses exhibit suppression of these features. The Hann pulse also exhibits a lower peak transition probability and broader central lobe than the square pulse for the same t_B, as expected from Fig. 4.3b.

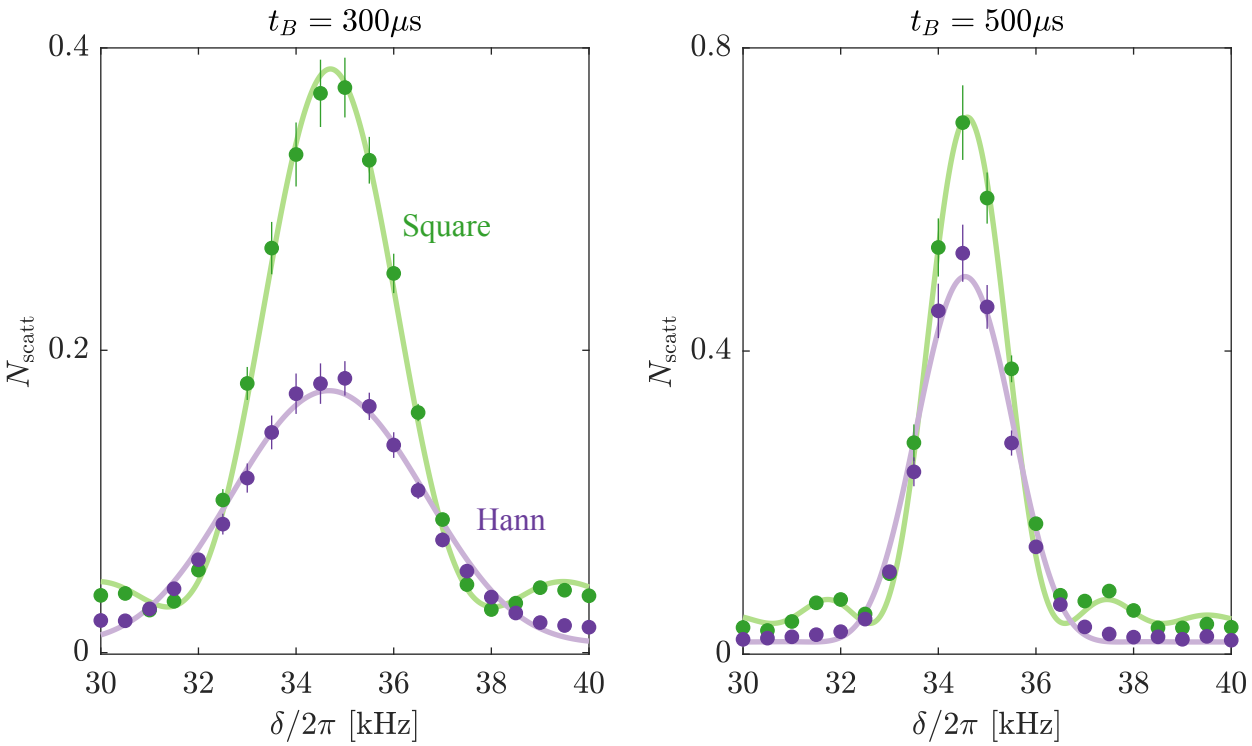

Figure 4.4: Spectral response of a stationary BEC. A stationary BEC is interrogated with Bragg pulses of square (green) and Hann (purple) pulseshape. Results are shown for $t_B = 300\,\mu$s (left) and $t_B = 500\,\mu$s. Solid lines show the expected spectral response from Eqs. 4.6 and 2.11. with fixed t_B and fitted amplitude and peaks. Sidelobes visible in the square pulseshape response are suppressed for the Hann pulseshape.

For both pulseshapes, the mean fitted δ_0 deviatesfrom the theoretical expectation by around $300\times 2\pi$ Hz. This is because we define δ_0 in Eq. 2.5 as the resonant detuning for stationary *free* atoms with a quadratic dispersion relation. In a BEC, however, atoms are not free particles, and the dispersion relation is given by Bogoliubov theory [46]. This results in the mean-field shift, $\delta_0 \to \delta_0 + \delta_{\text{MF}}$, which depends on the chemical potential μ ($\delta_{\text{MF}} = \frac{4}{7}\mu$) and is explored in more detail in [47].

This study demonstrates that we can indeed sculpt the spectral response to optimise spatial velocity field extraction. By probing with a Hann pulse of shorter duration we can achieve a spectral response with suppressed sidebands ideal for broadband velocimetry. We can utilise a square pulse of longer duration to generate a narrow spectral response for spectroscopic velocimetry, where sideband coupling is less critical.

5. Probing Velocity Fields

Building on the Bragg scattering experiments in Chapter 4, we turn to the crux of this thesis: extracting spatially-resolved velocity fields. We first characterise the velocity dependence of the Bragg resonance in a BEC with uniform velocity distribution. We then extract vortex-antivortex velocity fields using the *spectroscopic* and *broadband* introduced in Chapter 2. Finally, we apply the broadband method along two axes to reconstruct the full 2D velocity field of a far-from-equilibrium vortex gas.

5.1 Probing Uniform Velocity Fields

Before extracting spatially-resolved velocity fields, we first probe the velocity-dependence of the Bragg resonance by extracting the speed of condensates with uniform velocity fields. These configurations are deterministically produced using the phase imprinting method described in Section 1.1.2.

By pulsing far-detuned dipole laser light of linearly decreasing intensity, we impart a constant phase gradient [Eq. 1.6] and thus uniform velocity field [Eq. 1.1], illustrated in Fig. 5.1.

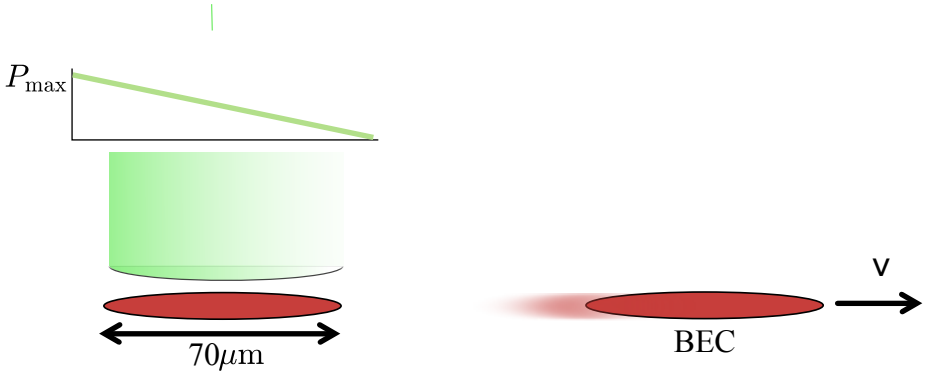

Figure 5.1: Producing uniform velocity fields with phase imprinting. The linearly decreasing beam intensity is generated using the DMD. The number of mirrors turned on are spatially decreased in the Bragg axis direction $\hat{\boldsymbol{x}}'$. The intensity gradient is set with the incident dipole laser power, $P_{\max}$. The intensity profile, illustrated on the left, is incident for $50\,\mu$s. This imprints a phase gradient on the BEC, which recoils with a uniform velocity v along the Bragg axis, illustrated on the right.

By selecting the incident DMD light power $P_{\max}$, we vary the phase gradient imprinted. After the imprint, DMD light is shut off, and the BEC is simultaneously probed with a Bragg pulse. After a 5 ms TOF, the atom distribution is measured, and we extract scattered fractions N_+/N_T and N_-/N_T using the method outlined in Fig. 4.1. This is repeated over a range of 2-photon detunings δ to find the velocity-dependent resonant Doppler detuning $\delta_d(v_\parallel)$. Results are shown in Fig. 5.2b.
For zero phase imprint ($P_{\max} = 0$), the fractions of upper and lower Bragg-scattered atoms are expected to be centred around $\delta = \delta_0$, the resonant 2-photon detuning for stationary atoms. However, resonances deviate from expectation $\delta_d = \pm 50\,$Hz respectively, revealing a small residual velocity component along the Bragg axis on the order $\sim 0.01\,\mu\text{m/ms}^{-1}$ [Eq.2.6]. As

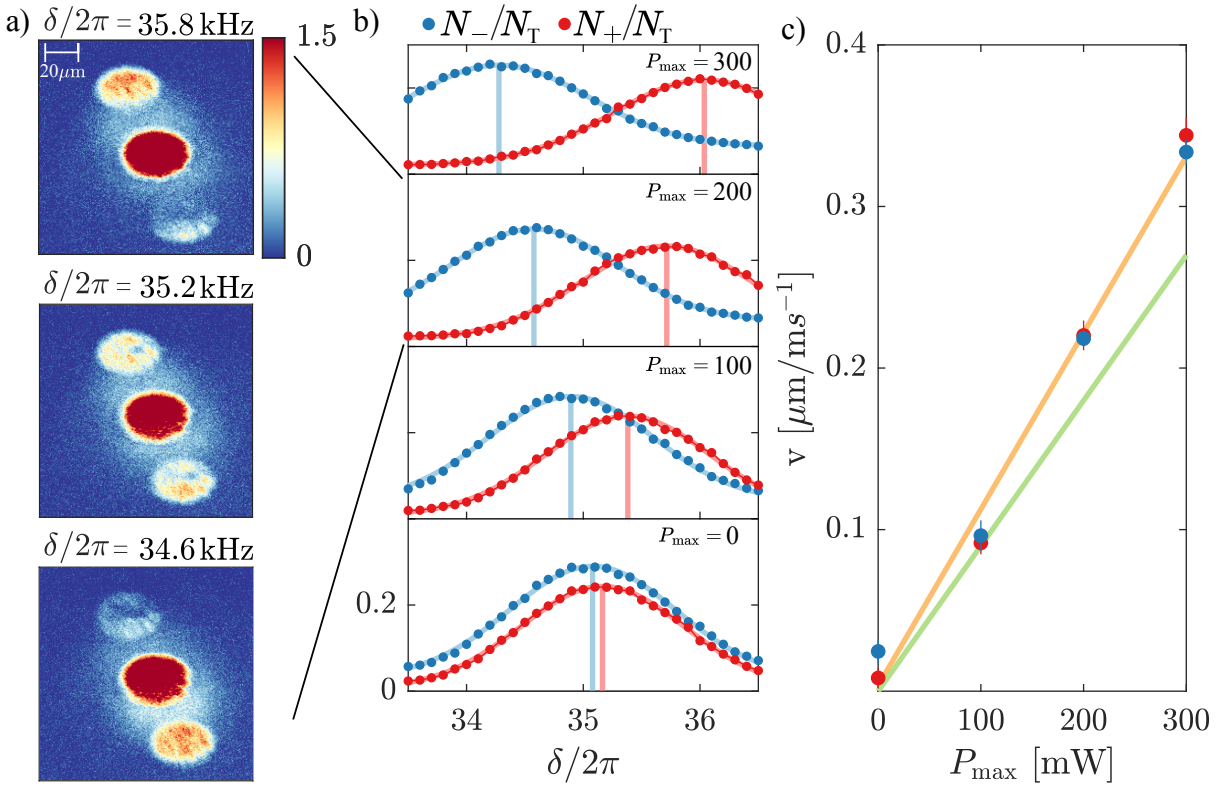

Figure 5.2: Uniform velocity field measurement. a) Atom distributions at $P_\mathrm{max} = 200\,\mathrm{mW}$. For $\delta/2\pi = 35.2\,\mathrm{kHz} \approx \delta_0$, scattering is symmetric with no velocity selection. For $\delta_d/2\pi = \pm 600\,\mathrm{Hz}$, scattering is velocity dependent, populating the upper and lower clouds asymmetrically about δ_0. Colorbars indicate atom number per pixel. **b)** Blue and red points show scattered fractions $N_\pm/N_T$ vs.δ. N_- is systematically offset from N_+ due to locally increased background noise. Vertical error bars are plotted, but smaller than the marker size. Solid lines are Gaussian fits used to extract resonant δ across P_max, indicated by vertical lines. **c)** Velocities calculated from upper and lower cloud Doppler detunings agree, and scale linearly with P_max. A linear fit (yellow) and prior calibration (green) are shown for comparison.

P_max is increased linearly, $\delta_d(v_\parallel)$ increases proportionally. The retroreflected Bragg pulse that couples atoms to the lower cloud probes velocity components in the opposite direction to the upper cloud-coupling Bragg pulse. Therefore, the resonance for velocity $v_\parallel$ is at $-\delta_d(v_\parallel)$. This is demonstrated by atom images in Fig. 5.2a.

Fig. 5.2c shows velocities extracted from $\delta_d(v_\parallel)$ for the upper and lower Bragg-scattered atoms. As expected, measured velocities increase linearly with P_max, demonstrated by the yellow line of best fit, and are consistent with prior calibration [21], shown by the green line. This validates the use of Bragg scattering for velocity extraction, forming the basis for spatially-resolved measurements in the following sections.

5.2 1D Spatial Velocity Fields: Vortex-Antivortex Pair

Section 2.3 introduced two distinct velocimetry methods. *Spectroscopic* velocimetry scans δ across multiple shots, extracting the spatially varying Doppler detuning $\delta_d(x, y; v_\parallel)$ by analysing each spatial bin independently. *Broadband* velocimetry infers $\delta_d(x, y; v_\parallel)$ in a single shot by comparing the local scattered fraction to a measured spectral response [Section 4.3]. We apply both methods to reconstruct the spatial velocity field of a vortex-antivortex pair (2 counterrotating vortices). Similar configurations have been investigated with Bragg scattering to identify vorticity [13, 17], however, the projected 1D velocity field $v_\parallel(x, y)$ has not been measured before.

5.2.1 Deterministic Vortex Production

Spectroscopic velocimetry can only be performed on reproducible velocity fields. To produce vortices deterministically, we employ the chopstick method [48], illustrated in Fig. 5.3.

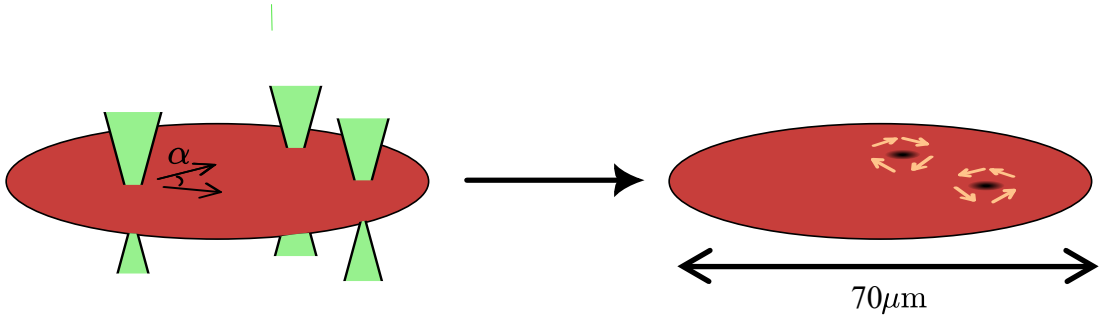

Figure 5.3: The chopstick method. A column of dipole laser light (green) pierces the quasi-2D BEC (red disc). The light is split, and two columns are translated linearly across the BEC at a speed of $3\,\mu\mathrm{m/m}s^{-1}$. On the left, the initial and final positions of the columns are illustrated. Black arrows show the direction of each column, diverging at an angle $\alpha \sim 30°$. In the final position, the intensities of the light columns are ramped to 0. This deposits two counterrotating vortices, illustrated on the right. Vortex positions are reproducible to the nearest $\pm 5\,\mu$m.

Axial far-detuned laser light pierces the trapped condensate and acts as a repulsive object [Eq. 1.2]. The light is split into two columns, which are simultaneously translated across the BEC, diverging with angle α. As the 'chopsticks' move, they create circular flows around them. For the right chopstick trajectory parameters, this results in 2 vortices of opposite phase windings $\pm 2\pi$ that are pinned at the position of the chopsticks. The chopsticks are then ramped to 0, depositing a vortex-antivortex pair of vorticities ± 1.

5.2.2 1D Velocity Field Extraction

We implement spectroscopic velocimetry by scanning δ of a Bragg pulse upward from δ_0. A long pulse duration of $t_B = 700\,\mu$s and square pulseshape is selected to generate a narrow spectral broadening of $1.5\,$kHz. t_B is not increased further in order to maintain spatial resolution [Fig. 4.2]. For each spatial bin, a spectral response profile is fitted, from which we can build the spatial distribution $\delta_{\mathrm{res}}(x_i, y_j)$. We find δ_0 from spectroscopy of a condensate where no vortices are produced, and extract $v_\parallel(x_i, y_j)$ using Eq. 2.3.

For broadband velocimetry, a single realisation of the vortex-antivortex configuration is Bragg-scattered using a fixed detuning $\delta = 36 \times 2\pi\,$kHz and a shorter pulse duration $t_B = 400\,\mu$s.

This yields a spectral width of $2.5\,$kHz that spans the expected range of Doppler detunings $\delta_d(v\|)$. At each spatial bin, the local scattered fraction in the upper and lower clouds is mapped to a reference spectral response. Inverting this response function gives two possible values for $\delta_{\text{res}}(x_i, y_j)$. The physical one is consistent across both scattered distributions. A Hann pulseshape is used to suppress sidelobes of the spectral response [Fig. 4.3].

The reference spectral response shape is obtained via Bragg spectroscopy of a flat condensate, as described in Section 4.3, and is measured separately for the upper and lower clouds. At the fixed detuning $\delta = 36 \times 2\pi\,$kHz, atoms with velocities corresponding to $\delta_d(v_\|) = \delta - \delta_0$ are maximally scattered to $n_+(x_i, y_j)$. Conversely, atoms satisfying $\delta_d(-v_\|) = \delta_0 - \delta$ are maximally scattered to $n_-(x_i, y_j)$. Atoms with Doppler detunings that are off-resonance are scattered with lower probabilities. Therefore, the measured lineshapes for the two clouds are shifted to be centred about $\delta_0 \pm (\delta - \delta_0)$ respectively to form the reference spectral responses. For the stationary condensate, the resonance condition for each scattering direction is the same, and the scattered fraction is halved between the clouds. At $\delta = 36 \times 2\pi\,$kHz, the resonance is velocity dependent, and scattering in each direction is not equal. To account for this, the reference responses for the upper and lower clouds are scaled such that their combined total scattered fraction at resonance matches that of the stationary condensate.

We extract spatially-resolved 1D velocity fields for 2 different vortex-antivortex configurations via both spectroscopic and broadband velocimetry. Each measurement is compared to theoretical expectations obtained from a 2D numerical Gross-Pitaevskii equation (GPE) solver, where vortices are initialised with phase windings and Gaussian density dips. After imaginary time evolution, the solver converges on a stable vortex configuration. Results are shown in Fig. 5.4.

For both velocimetric methods, the density fields are constructed by summing the distributions of the scattered and unscattered clouds, which are extracted using the method discussed in Section 4.1. These are shown in Figs. 5.4a and e. Figs. 5.4b-d and f-h correspond to the respective theoretical and extracted 1D velocity fields.

Qualitatively, the measured velocity fields agree with theoretical expectation. This is shown quantitatively in lineouts plotted in Figs. 5.4i and j. One clear difference between the extracted fields is the absence of the diverging velocities near the vortex core. This is due to low atom densities at the cores that cannot be resolved. By convoluting the theoretical prediction with the experimental spatial binning, the measured velocities at these positions could be compared with theory more suitably.

The lineouts of the velocity fields extracted from the spectroscopic and broadband methods are in good agreement with each other. Fluctuation in the broadband lineouts arise from uncertainty in the atom number, and should be investigated further by comparing multiple extracted velocity fields for the same configuration. The larger positive velocities measured by the broadband method in Fig. 5.4j is likely due to vortices in the single realisation being slightly closer together, thus increasing velocity between the vortices.

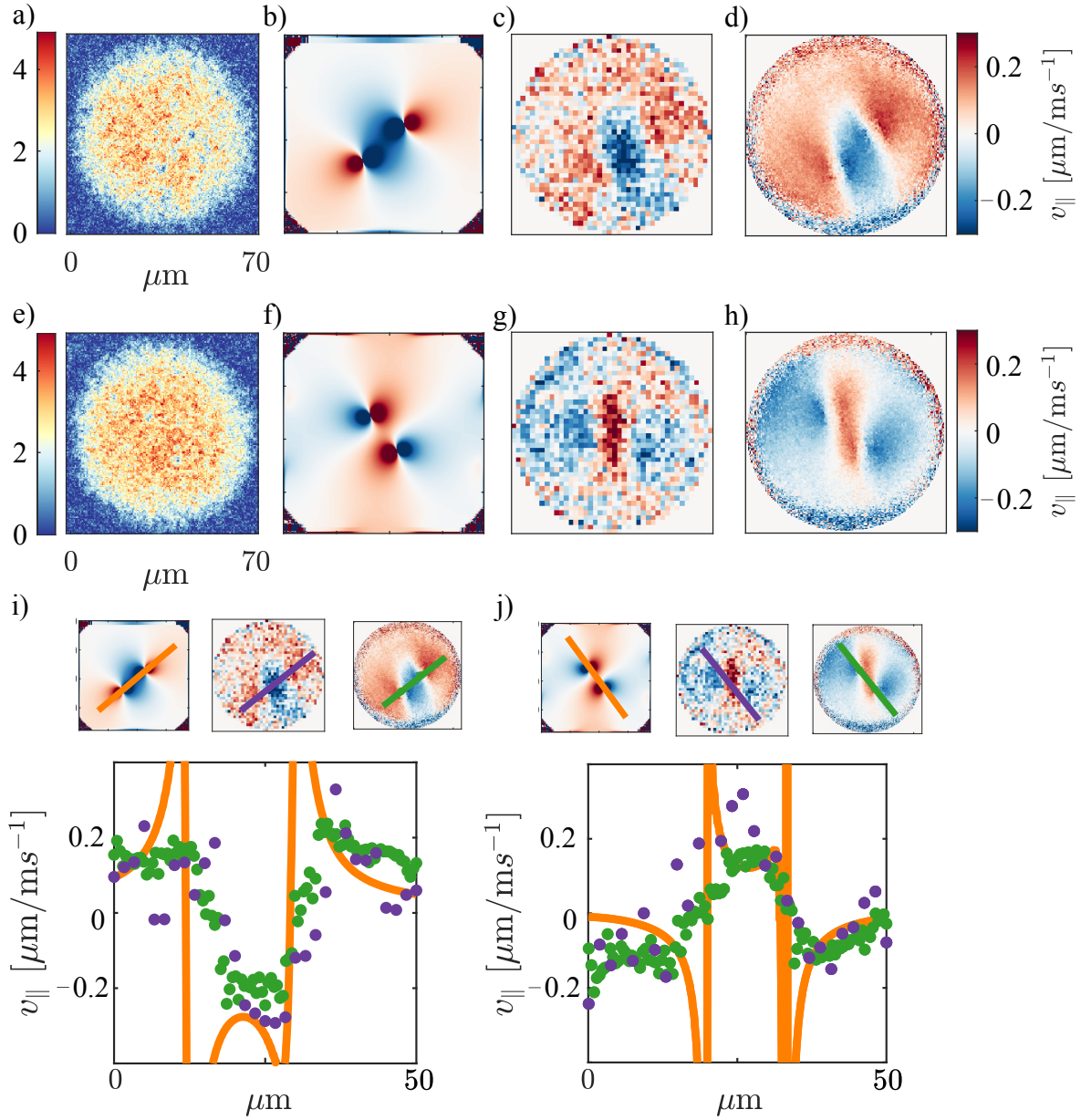

Figure 5.4: 1D velocity fields for vortex-antivortex configurations. **a)** Single realisation of atom density, reconstructed by summing scattered and unscattered clouds from broadband velocimetry. The colorbar indicates atoms per pixel. 2 large density dips can be identified as vortices, but no information on vorticity is available. **b)** Theoretical expectation calculated computationally with a numerical 2D GPE solver, where vortices are added synthetically. **c)** $v_\parallel(x_i, y_j)$ extracted via broadband velocimetry from a single realisation. A 2x2 (pixels) spatial bin size is determined as the minimum bin size for which the method converges on a velocity field. **d)** $v_\parallel(x_i, y_j)$ extracted via spectroscopic velocimetry, where $\delta/2\pi$ is scanned in steps of 200 Hz from 34.2 kHz to 38 kHz and averaged over 12 times for each δ. Shots where vortices are not formed as expected are manually discarded. **e-h)** Atom density, theoretical expectation, broadband $v_\parallel(x_i, y_j)$, and spectroscopic $v_\parallel(x_i, y_j)$ for a different vortex-antivortex configuration. **i-j)** Lineouts of b-d) and f-h), respectively, along the vortex cores. Lineout paths are shown in the upper 3 plots. Spectroscopic (green) and broadband (purple) methods are in agreement with theoretical expectation (orange). High velocities near vortex cores are not resolved due to low atom densities.

Key differences in the methods are captured in the extracted velocity fields. For the broadband method, larger spatial bins are used for velocity field reconstruction. This is due to the method's direct dependence on measuring the atom density, which is more stable when averaged over a larger area. The spectroscopic method extracts large velocities at the edges of the condensate that are independent of the vortex condfguration. This is due to the ballistic expansion of the atoms, discussed previously in Section 4.2. This is not seen in the broadband method because these large velocities correspond to Doppler detunings with couple minimally to the Bragg pulse. A smaller pulse duration increases the range of velocities visible, but decreases velocity resolution.

5.3 2D Spatial Velocity Fields: Vortex Gas

In the experimental setup outlined in Chapter 2, we implement another independent beam axis at an angle $\theta = 47°$ from the axis used in previous sections. With this, we simultaneously extract the spatially-resolved velocity components along the 2 axes to construct the full 2D vector velocity field map of a turbulent, far-from-equilibrium vortex gas configuration. In this section, we present initial results, and outline key limitations that must be investigated in more detail.

The turbulent vortex gas is produced by translating a paddle with a $20\,\mu$m slit through a square condensate. This is analogous to quickly swiping such a paddle through water, and is illustrated in Fig. 5.5.

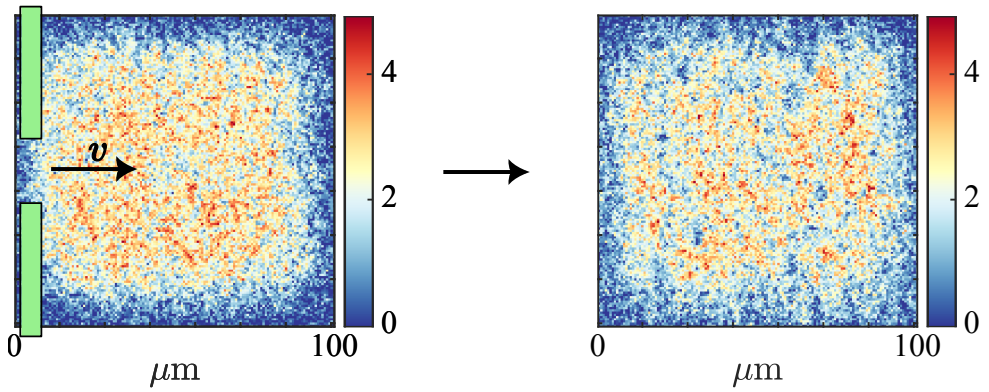

Figure 5.5: Producing turbulent, far-from-equilibrium configurations. The DMD is used to produce a paddle of dipole laser light with a 20μ m slit which is translated across a square BEC at a speed of $v = 3\,\mu\text{m/m}s^{-1}$. This is illustrated on the left with a spatial atom distribution of a single equilibrated realisation. A single realisation of the resulting turbulent, irreproducible vortex gas configuration shown on the right. Colorbars indicate number of atoms per pixel.

The configuration is interrogated with retroreflected Bragg pulses along the two beam axes, resulting in 4 scattered clouds, shown in Fig. 5.6a. The spatial atom distributions of the scattered and unscattered clouds are extracted using a modified version of the method described in Section 4.1. The two components of the velocity field are extracted in a single shot via broadband velocimetry, using reference spectral responses calibrated for each cloud with the protocol described in the previous section. For turbulent, irreproducible configurations, velocity field extraction with spectroscopic velocimetry is not possible.

The resulting extracted 1D velocity fields are shown in Fig. 5.6b. The density profile is reconstructed by summing the scattered and unscattered atom distributions and is shown in Fig. 5.6d.

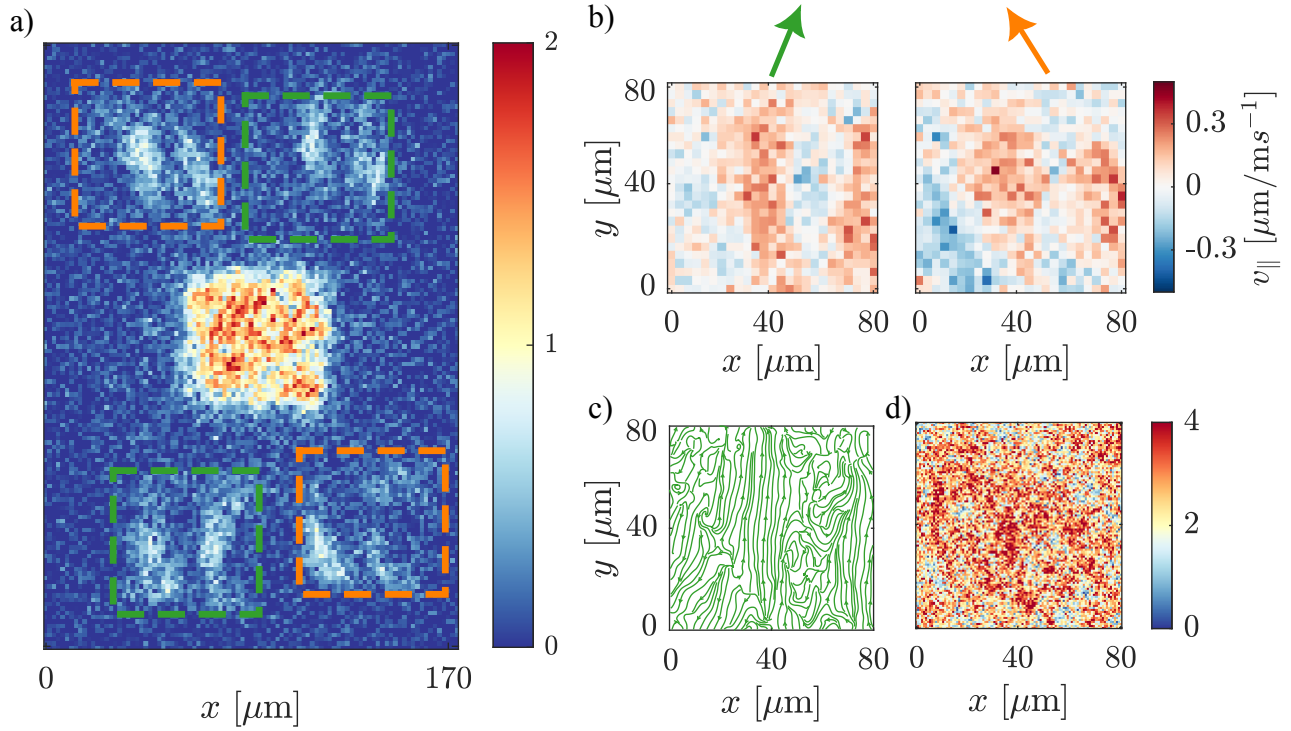

Figure 5.6: 2D velocity field for a turbulent vortex gas configuration. **a)** The spatial atom distribution of a quasi-2D vortex gas configuration probed with Bragg pulses of $\delta = 2\pi \times 36\,\mathrm{kHz}$ and $t_B = 400\,\mu\mathrm{s}$, imaged after $t_{\mathrm{TOF}} = 5\,\mathrm{ms}$. The colorbar shows atoms per pixel. Bragg pulses along the two axes are triggered simultaneously, and result in scattered clouds along 2 axes at an angle of $47°$. **b)** The velocity fields $v_{\parallel}(x_i, y_j)$ along the two axes are plotted, where the colour of the arrow above corresponds to the scattered clouds analysed, and the direction corresponds to the Bragg axis direction. **c)** Streamline velocity plot made by combining the two velocity projections into a 2D vector field. Produced in MATLAB. **d)** Reconstructed density distribution by summing scattered and unscattered spatial atom distributions. Spatial resolution is set by pixel size, whereas a) and b) are 2x2 binned.

By decomposing the velocity components into a perpendicular basis, we build a spatially-resolved 2D velocity field. In Fig. 5.6c, we interpolate between extracted velocity vectors to produce a streamline plot. Here, the velocity field has curl at certain positions, while having straight bulk flow at others. Some regions of curl overlap with density dips in Fig. 5.6d. Whilst this is characteristic of a vortex gas, more analysis should be done to confirm the method's efficacy.

It is unclear how well the assumption of independence of the beam axes holds. This could be investigated further by a calibration measurement where uniform velocities with different directions are probed in 2 axes. Vortices identified from regions of high curl in the interpolated streamline velocity field could be used to compute a theoretical expectation of the velocity field. Additionally, we can search for signs of previously established quantum vortex dynamics such as Onsager cluster formation [49]. The direct comparison with expected results based on theory and previous experiment would provide a good test for the physicality of 2D velocity field extraction using broadband velocimetry.

6. Conclusion and Outlook

In this thesis, we implement an experimental setup capable of Bragg scattering, where all beam parameters can be controlled by the main experimental control software. The setup allows for the production of Bragg pulses with arbitrary positive-valued pulseshapes, enabling the spectral response to be engineered for the first time in Bragg-based velocimetry. The Bragg scattering setup is charaterised with an equilibrated BEC with an approximately flat phase profile, with which Rabi oscillations and the spectral response are measured. Bragg scattering velocity-dependence is demonstrated by probing BECs with constant phase gradients.

We present two novel methods that can be used to extract spatially-resolved velocity fields from quasi-2D BECs: *spectroscopic* velocimetry, where different velocities are probed over a range of destructive measurements; and *broadband* velocimetry, where the velocity field is measured in a single shot, enabling the velocity field extraction of irreproducible BEC configurations. These methods are succesfully demonstrated to measure the velocity field of a vortex-antivortex system, with results in good agreement with theory. The spatial resolution of spectroscopic velocimetry depends primarily on the reproducibility of the BEC configuration. Velocity resolution increases with the Bragg pulse duration, however, this comes at the sacrifice of spatial resolution. Both the spatial and velocity resolution of broadband velocimetry depend on the accuracy of the atom density measurement. For the vortex-antivortex system, we find the broadband velocimetry spatial resolution is larger than the spectroscopic method by a factor 4. The range of velocities sensitive to broadband velocimetry depends on the minimum atom density that can be differentiated from noise and the velocity resolution depends on the ability to resolve atom number densities. Both can be optimised by increasing the number of atoms in the system.

By performing Bragg scattering along 2 axes, we apply the newfound method of broadband velocimetry to extract a 2D vector velocity field of a more turbulent vortex gas system. We present initial results, however further investigation is required to verify the physicality of the extraction. It would be insightful to compare results with computational expectation and perform additional calibratory experiments to confirm the accuracy of measured velocity directions.

Before the velocimetry methods can be added to the toolkit for probing far-from-equilibrium BEC, the precision of velocity field extraction should be quantified. This can be achieved by comparing extracted velocity fields from a reproducible system. However, a challenge arises in differentiating fluctuations due to shot-to-shot configurational differences from the uncertainty of the velocimetry. The spatial resolution can be quantified by extracting the velocity field of a system with distinct spatial structure, such as a phase gradient in a finite region. For both methods, we expect a relatively large source of error to come from power fluctuations in laser light used for Bragg scattering, resulting in a maximum scattered atom number fluctuation of 7.8%. This can be reduced by implementing PI-based power stabilisation.

The Bragg scattering setup also has applications outside of velocity field extraction. Its use as an atomic beam splitter is applicable for measurements of quantum entanglement [50]. Additionally, the Bragg pulse could be implemented as a velocity filter, removing atoms of

a particular velocity from the system. One final, especially interesting question for analog quantum simulation performed at BECK is how Bragg scattering can be used as a method of interacting with phonons.

Bibliography

[1] M. H. Anderson, J. R. Ensher, M. R. Matthews, C. E. Wieman, and E. A. Cornell, "Observation of bose-einstein condensation in a dilute atomic vapor," *Science*, vol. 269, no. 5221, pp. 198–201, 1995.

[2] E. A. L. Henn, J. A. Seman, G. Roati, K. M. F. Magalhães, and V. S. Bagnato, "Emergence of turbulence in an oscillating bose-einstein condensate," *Phys. Rev. Lett.*, vol. 103, no. 4, p. 045301, 2009.

[3] T. W. Neely *et al.*, "Characteristics of two-dimensional quantum turbulence in a compressible superfluid," *Phys. Rev. Lett.*, vol. 111, no. 23, p. 235301, 2013.

[4] W. J. Kwon, G. Moon, J. Choi, S. W. Seo, and Y. Shin, "Relaxation of superfluid turbulence in highly oblate bose-einstein condensates," *Phys. Rev. A*, vol. 90, no. 6, p. 063627, 2014.

[5] N. Navon, A. L. Gaunt, R. P. Smith, and Z. Hadzibabic, "Emergence of a turbulent cascade in a quantum gas," *Nature*, vol. 539, pp. 72–75, 2016.

[6] A. N. Kolmogorov, "Dissipation of energy in the locally isotropic turbulence," *Proceedings of the Royal Society of London. Series A, Mathematical and Physical Sciences*, vol. 434, no. 1890, pp. 9–13, 1991.

[7] P. Anderson, "Considerations on the flow of superfluid helium," *Reviews of Modern Physics*, vol. 38, pp. 298–310, 1966.

[8] G. Blatter, M. V. Feigel'man, V. B. Geshkenbein, A. I. Larkin, and V. M. Vinokur, "Vortices in high-temperature superconductors," *Reviews of Modern Physics*, vol. 66, pp. 1125–1388, 1994.

[9] B. Haskell and A. Melatos, "Models of pulsar glitches," *International Journal of Modern Physics D*, vol. 24, no. 3, p. 1530008, 2015.

[10] S.-H. Shinn and A. del Campo, "Electrodynamics of vortices in quasi-two-dimensional scalar bose-einstein condensates," *Physical Review Research*, vol. 7, no. 1, p. 013217, 2025.

[11] S.-C. Tung, G. Lamporesi, D. Lobser, L. Xia, and E. A. Cornell, "Observation of the presuperfluid regime in a two-dimensional bose gas," *Physical Review Letters*, vol. 105, p. 230408, Dec. 2010.

[12] S. R. Muniz, D. Naik, and C. Raman, "Bragg spectroscopy of vortex lattices in bose-einstein condensates," *Physical Review A*, vol. 73, p. 041605, 2005.

[13] S. W. Seo, B. Ko, J. H. Kim, and Y. Shin, "Observation of vortex-antivortex pairing in decaying 2d turbulence of a superfluid gas," *Scientific Reports*, vol. 7, 2017.

[14] S. P. Johnstone, A. J. Groszek, P. T. Starkey, C. J. Billington, T. P. Simula, and K. Helmerson, "Evolution of large-scale flow from turbulence in a two-dimensional superfluid," *Science*, vol. 364, no. 6447, pp. 1267–1271, 2019.

[15] P. B. Blakie and R. Ballagh, "Spatially selective bragg scattering: a signature for vortices in bose-einstein condensates.," *Physical review letters*, vol. 86 18, pp. 3930–3, 2001.

[16] G. Gauthier *et al.*, "Giant vortex clusters in a two-dimensional quantum fluid," *Science*, vol. 364, no. 6447, pp. 1264–1267, 2019.

[17] W. J. Kwon *et al.*, "Sound emission and annihilations in a programmable quantum vortex collider," *Nature*, vol. 600, pp. 64–69, 2021.

[18] C. Chin, R. Grimm, P. Julienne, and E. Tiesinga, "Feshbach resonances in ultracold gases," *Reviews of Modern Physics*, vol. 82, pp. 1225–1286, Apr. 2010.

[19] C. Viermann *et al.*, "Quantum field simulator for dynamics in curved spacetime," *Nature*, vol. 611, no. 7935, pp. 260–264, 2022.

[20] M. Sparn *et al.*, "Experimental particle production in time-dependent spacetimes: A one-dimensional scattering problem," *Physical Review Letters*, vol. 133, p. 260201, Dec. 2024.

[21] N. Liebster *et al.*, "Observation of pattern stabilization in a driven superfluid," *Physical Review X*, vol. 15, no. 1, p. 011026, 2025.

[22] N. Liebster *et al.*, "Supersolid-like sound modes in a driven quantum gas," *Nature Physics*, vol. in press, 2025.

[23] M. Hans, *Physical Computing on a Versatile Setup for Ultra-cold Potassium*. Phd thesis, Universität Heidelberg, 2022.

[24] R. Grimm, M. Weidemüller, and Y. B. Ovchinnikov, "Optical dipole traps for neutral atoms," *Advances in Atomic, Molecular, and Optical Physics*, vol. 42, pp. 95–170, 2000.

[25] M. Sparn, "A setup for creating arbitrary potentials in a two-dimensional ^{39}k bec with a digital micromirror device," master thesis, Universität Heidelberg, 2020.

[26] F. Dalfovo, S. Giorgini, L. P. Pitaevskii, and S. Stringari, "Theory of bose–einstein condensation in trapped gases," *Reviews of Modern Physics*, vol. 71, no. 3, pp. 463–512, 1999.

[27] L. Brillouin, *Wave Propagation in Periodic Structures: Electric Filters and Crystal Lattices*. New York: Dover Publications, 2nd ed., 1953.

[28] F. Bloch, "On the quantum mechanics of electrons in crystal lattices," *Zeitschrift für Physik*, vol. 52, no. 7–8, pp. 555–600, 1928.

[29] E. Arimondo, H. Lew, and T. Oka, "Deflection of a na beam by resonant standing-wave radiation," *Physical Review Letters*, vol. 43, no. 11, pp. 753–756, 1979.

[30] V. A. Grinchuk *et al.*, "Title unknown," *Physics Letters A*, vol. 86, pp. 136–138, 1981.

[31] P. L. Gould, G. A. Rou, and D. E. Pritchard, "Diffraction of atoms by light: The near-resonant kapitza-dirac effect," *Physical Review Letters*, vol. 56, no. 8, pp. 827–830, 1986.

[32] J.-Y. Courtois, G. Grynberg, B. Lounis, and P. Verkerk, "Recoil-induced resonances in cesium – an atomic analog to the free-electron laser," *Physical Review Letters*, vol. 72, no. 20, pp. 3017–3020, 1994.

[33] M. Kozuma *et al.*, "Coherent splitting of bose-einstein condensed atoms with optically induced bragg diffraction," *Physical Review Letters*, vol. 82, no. 5, pp. 871–875, 1999.

[34] H. Biss *et al.*, "Excitation spectrum and superfluid gap of an ultracold fermi gas," *Physical Review Letters*, vol. 131, no. 3, p. 035302, 2023.

[35] H. Müller, S.-w. Chiow, Q. Long, S. Herrmann, and S. Chu, "Atom interferometry with up to 24-photon-momentum-transfer beam splitters," *Physical Review Letters*, vol. 100, no. 18, p. 180405, 2008.

[36] D. Suter, *The Physics of Laser-Atom Interactions*. Cambridge, UK: Cambridge University Press, 1997.

[37] A. Béguin, T. Rodzinka, L. Calmels, B. Allard, and A. Gauguet, "Atom interferometry with coherent enhancement of bragg pulse sequences," *Physical Review Letters*, vol. 131, no. 14, p. 143401, 2023.

[38] J. J. Sakurai, *Modern Quantum Mechanics*. Reading, MA: Addison-Wesley, revised edition ed., 1994.

[39] C. Leprince *et al.*, "Coherent coupling of momentum states: Selectivity and phase control," *Physical Review A*, vol. 111, no. 6, p. 063304, 2025.

[40] I. I. Rabi, "Space quantization in a gyrating magnetic field," *Physical Review*, vol. 51, no. 8, pp. 652–654, 1937.

[41] T. G. Tiecke, "Properties of potassium," 2019. Unpublished notes on various properties of Potassium relevant for ultracold gases experiments.

[42] G. H. Zhang, B. Braverman, A. Kawasaki, and V. Vuletić, "Fast compact laser shutter using a direct current motor and 3d printing," *Review of Scientific Instruments*, vol. 86, no. 12, p. 126105, 2015.

[43] M. Hans *et al.*, "High signal to noise absorption imaging of alkali atoms at moderate magnetic fields," *Review of Scientific Instruments*, vol. 92, no. 2, p. 023203, 2021.

[44] A. Nuttall, "Some windows with very good sidelobe behavior," *IEEE Transactions on Acoustics, Speech, and Signal Processing*, vol. 29, no. 1, pp. 84–91, 1981.

[45] J. O. S. III, *Spectral Audio Signal Processing*. Center for Computer Research in Music and Acoustics (CCRMA), Stanford University, 2011.

[46] C. J. Pethick and H. Smith, *Bose-Einstein Condensation in Dilute Gases*. Cambridge: Cambridge University Press, 2nd ed., 2008.

[47] J. Stenger, S. Inouye, A. P. Chikkatur, D. M. Stamper-Kurn, D. E. Pritchard, and W. Ketterle, "Bragg spectroscopy of a bose-einstein condensate," *Phys. Rev. Lett.*, vol. 82, pp. 4569–4573, Jun 1999.

[48] E. C. Samson, K. E. Wilson, Z. L. Newman, and B. P. Anderson, "Deterministic creation, pinning, and manipulation of quantized vortices in a bose-einstein condensate," *Physical Review A*, vol. 93, no. 2, p. 023603, 2016.

[49] L. Onsager, "Statistical hydrodynamics," *Il Nuovo Cimento (1943-1954)*, vol. 6, pp. 279–287, 1949.

[50] C. Gross, T. Zibold, E. Nicklas, J. Estève, and M. K. Oberthaler, "Nonlinear atom interferometer surpasses classical precision limit," *Nature*, vol. 464, pp. 1165–1169, 2010.